The Development of the North Pacific Jet Phase Diagram as an Objective Tool to Monitor the State of the Upper-Tropospheric Flow Pattern

By

ANDREW C. WINTERS[1*], DANIEL KEYSER[1], and LANCE F. BOSART[1]

[1]Department of Atmospheric and Environmental Sciences
University at Albany, State University of New York
Albany, NY 12222

Submitted for publication in *Weather and Forecasting*
21 June 2018

Revised version submitted
10 October 2018

[*] *Corresponding author address:* Andrew C. Winters, Dept. of Atmospheric and Environmental Sciences, University at Albany, SUNY, 1400 Washington Ave., Albany, NY 12222. E-mail: acwinters@albany.edu

ABSTRACT

Previous studies employing empirical orthogonal function (EOF) analyses of upper-tropospheric zonal wind anomalies have identified the leading modes of North Pacific jet (NPJ) variability that prevail on synoptic time scales. The first mode corresponds to a zonal extension or retraction of the exit region of the climatological NPJ, while the second mode corresponds to a poleward or equatorward shift of the exit region of the climatological NPJ. These NPJ regimes can strongly influence the character of the large-scale flow pattern over North America. Consequently, knowledge of the prevailing NPJ regime and the forecast skill associated with each NPJ regime can add considerable value to operational medium-range (6–10-day) forecasts over North America.

This study documents the development of an NPJ Phase Diagram, which is constructed from the two leading EOFs of 250-hPa zonal wind anomalies during 1979–2014 excluding the summer months (Jun–Aug). The projection of 250-hPa zonal wind anomalies at one or multiple times onto the NPJ Phase Diagram provides an objective characterization of the state or evolution of the upper-tropospheric flow pattern over the North Pacific. A 30-year analysis of GEFS reforecasts with respect to the NPJ Phase Diagram demonstrates that forecasts verified during jet retraction and equatorward shift regimes are associated with significantly larger average errors than jet extension and poleward shift regimes. An examination of the best and worst forecasts further suggests that periods characterized by rapid NPJ regime transition and the development and maintenance of North Pacific blocking events exhibit reduced forecast skill.

1. Introduction

Anchored downstream of the Asian continent at middle latitudes, the North Pacific jet (NPJ) stream is a narrow, meandering current of strong upper-tropospheric wind speeds bounded by appreciable horizontal and vertical shear. The position and intensity of the NPJ is modulated by a number of external factors, including tropical convection (e.g., Hoskins and Karoly 1981; Madden and Julian 1994; Harr and Dea 2009; Archambault et al. 2013, 2015; Torn and Hakim 2015; Grams and Archambault 2016; Bosart et al. 2017), interactions between the NPJ and baroclinic eddies along the midlatitude storm track (e.g., Orlanski and Sheldon 1995; Chang et al. 2002; Hakim 2003; Torn and Hakim 2015; Bosart et al. 2017), and the East Asian Winter Monsoon (e.g., Jhun and Lee 2004; Lee et al. 2010; Wang and Chen 2014; Handlos and Martin 2016). In combination, these factors contribute to NPJ configurations that vary substantially on both weather and climate time scales.

In an attempt to characterize the variability of the NPJ, prior work has identified the leading modes of NPJ variability that prevail on weather and climate time scales during the winter (Dec–Feb). Schubert and Park (1991) provided one of the first investigations of subseasonal NPJ variability, and calculated the two leading traditional empirical orthogonal functions[1] (EOFs) of 20–70-day filtered zonal wind at 200 hPa over the Pacific basin. Their first EOF describes variability in the intensity of the NPJ over the western North Pacific, while their second EOF describes a zonal extension or retraction of the exit region of the climatological NPJ. In contrast, Eichelberger and Hartmann (2007) employed daily zonal wind data during January in their traditional EOF analysis and found that the first EOF of the vertically averaged zonal-mean zonal wind over the North Pacific encompasses variability in the intensity,

[1] A traditional EOF analysis is a statistical technique to extract patterns that explain the greatest fraction of the variance within a multidimensional dataset (Wilks 2011, chapter 12).

89 longitudinal extent, and latitudinal position of the NPJ. Consequently, the Eichelberger and
90 Hartmann (2007) analysis suggests that NPJ variability is considerably more complex when
91 analyzed on synoptic rather than subseasonal time scales.

92 Recent studies by Athanasiadis et al. (2010) and Jaffe et al. (2011) provided additional
93 physical clarity on the two leading modes of NPJ variability that prevail on synoptic time scales
94 during the cold season (Nov–Mar). These studies applied traditional EOF analysis to unfiltered
95 upper-tropospheric zonal wind data over the North Pacific and determined that the first mode of
96 NPJ variability corresponds to longitudinal variability in the vicinity of the exit region of the
97 climatological NPJ. Specifically, a positive EOF 1 pattern (+EOF 1) describes a zonal extension
98 of the exit region of the climatological NPJ, while a negative EOF 1 pattern (–EOF 1) describes a
99 zonal retraction of the exit region of the climatological NPJ. The second mode of NPJ variability
100 corresponds to latitudinal variability in the vicinity of the exit region of the climatological NPJ.
101 In the context of this mode, a positive EOF 2 pattern (+EOF 2) describes a poleward shift of the
102 exit region of the climatological NPJ, while a negative EOF 2 pattern (–EOF 2) describes an
103 equatorward shift.

104 Knowledge of the four NPJ configurations identified by Athanasiadis et al. (2010) and
105 Jaffe et al. (2011), hereafter referred to as NPJ regimes, subsequently permits an examination of
106 the relationship between each NPJ regime and the downstream large-scale flow pattern over
107 North America. To this end, Griffin and Martin (2017) employed time-extended EOF analyses
108 (e.g., Weare and Nasstrom 1982; Wilks 2011, chapter 12) of 250-hPa zonal wind data from the
109 NCEP/NCAR reanalysis dataset (Kalnay et al. 1996) to construct composite analyses of the
110 large-scale flow evolution over the North Pacific and North America during the 10-day period
111 preceding and following the development of each NPJ regime. The Griffin and Martin (2017)

112 analysis yields a clear relationship between each NPJ regime and the large-scale flow pattern
113 over North America, and implies that knowledge of the prevailing NPJ regime may add
114 considerable value to operational medium-range (6–10-day) forecasts of temperature and
115 precipitation over North America. However, this value is limited operationally without
116 complementary knowledge of the relative forecast skill associated with the development or
117 persistence of each NPJ regime.

118 The concept of regime-dependent forecast skill has been explored with respect to large-
119 scale upper-tropospheric flow regimes over the North Atlantic basin (e.g., Ferranti et al. 2015)
120 and with respect to large-scale atmospheric teleconnection patterns (e.g., Palmer 1988; Lin and
121 Derome 1996; Sheng 2002; Ferranti et al. 2015). While the configuration of midlatitude jet
122 streams can be closely related to atmospheric teleconnection patterns (e.g., Wettstein and
123 Wallace 2010; Woollings et al. 2010; Madonna et al. 2017), a study that examines regime-
124 dependent forecast skill over the North Pacific with respect to the leading modes of NPJ
125 variability on synoptic time scales has not been conducted. Consequently, a primary goal of the
126 present study is to identify whether certain NPJ regimes exhibit enhanced or reduced forecast
127 skill. In an effort to address this goal, the results from prior studies on NPJ variability (e.g.,
128 Athanasiadis et al. 2010; Jaffe et al. 2011; Griffin and Martin 2017) are extended to the cool
129 season (Sep–May) and a two-dimensional phase diagram, hereafter referred to as the NPJ Phase
130 Diagram, is developed employing the two leading modes of NPJ variability during that time
131 period. The NPJ Phase Diagram subsequently aids in visualizing the state and evolution of the
132 upper-tropospheric flow pattern over the North Pacific, and serves as an objective tool from
133 which new insights can be derived regarding the climatology and forecast skill of each NPJ
134 regime.

The remainder of this manuscript is structured as follows. Section 2 discusses the development of the NPJ Phase Diagram. Section 3 discusses the climatology of each NPJ regime and reviews the large-scale flow patterns associated with each NPJ regime. Section 4 examines the forecast skill of each NPJ regime with respect to the NPJ Phase Diagram. Section 5 illuminates the characteristics of the best and worst medium-range forecast periods with respect to the NPJ Phase Diagram, and section 6 offers a discussion of the results and some conclusions.

2. Development of the NPJ Phase Diagram

The NPJ Phase Diagram is developed utilizing anomalies of the zonal component of the 250-hPa vector wind from the 0.5°-resolution National Centers for Environmental Prediction Climate Forecast System Reanalysis (CFSR; Saha et al. 2010, 2014) at 6-h intervals during 1979–2014 excluding the summer months (Jun–Aug). The CFSR is chosen for this study because of its role in providing the initial conditions for the Global Ensemble Forecast System (GEFS) Reforecast Version 2 dataset prior to 2011 (Hamill et al. 2013). The GEFS Reforecast dataset is utilized in sections 4 and 5 to examine the forecast skill of each NPJ regime with respect to the NPJ Phase Diagram. 250-hPa zonal wind anomalies are calculated as the deviation of the instantaneous 250-hPa zonal wind from a 21-day running mean centered on each analysis time in order to remove the 36-year mean as well as the annual and diurnal cycles. The 21-day running mean at a particular analysis time is calculated from 250-hPa zonal wind data taken at 24-h intervals within a 21-day window centered on the analysis time for every year during 1979–2014. A traditional EOF analysis (Wilks 2011, chapter 12) is subsequently performed on the 250-hPa zonal wind anomaly data[2] within a horizontal domain bounded in latitude from 10°N to 80°N and in longitude from 100°E to 120°W in order to identify the two leading modes of NPJ

[2] 250-hPa zonal wind anomalies are weighted by the square root of their associated gridcell area prior to the application of traditional EOF analysis.

157 variability. This horizontal domain is chosen to encompass the North Pacific basin and to match
158 the domain employed by Griffin and Martin (2017).

159 In comparison to traditional EOF analysis, Griffin and Martin (2017) demonstrate that
160 time-extended EOF analysis (e.g., Weare and Nasstrom 1982; Wilks 2011, chapter 12) of 250-
161 hPa zonal wind anomalies over the North Pacific is beneficial for ensuring that the evolution of
162 the NPJ is characterized by a higher degree of temporal coherence. However, this higher degree
163 of temporal coherence is achieved by filtering out the high-frequency variability of the NPJ that
164 occurs on daily time scales (Griffin and Martin 2017; their Fig. 1). When considering the NPJ
165 and its influence on the downstream upper-tropospheric flow pattern over North America, short-
166 term fluctuations in the position, intensity, and evolution of the NPJ, such as those associated
167 with recurving tropical cyclones or intensifying extratropical cyclones, can have substantial
168 impacts on the character of the downstream upper-tropospheric flow pattern over North America
169 (e.g., Archambault et al. 2015; Torn and Hakim 2015; Grams and Archambault 2016; Bosart et
170 al. 2017). Additionally, the application of time-extended EOF analysis is computationally more
171 expensive than traditional EOF analysis, especially when employing a dataset with 0.5°
172 resolution such as the CFSR. For these two reasons, traditional EOF analysis is chosen for this
173 study. The subsequent analysis demonstrates that the application of traditional EOF analysis to
174 250-hPa zonal wind anomalies from the CFSR during the cool season produces the same two
175 leading modes of NPJ variability as found in previous studies (Athanasiadis et al. 2010; Jaffe et
176 al. 2011; Griffin and Martin 2017).

177 The regression of 250-hPa zonal wind anomaly data from the CFSR onto the first two
178 standardized principal components (PCs), PC 1 and PC 2, obtained from the traditional EOF
179 analysis reveals the spatial structures of EOF 1 and EOF 2 (Figs. 1a and 1b, respectively). EOF 1

explains 10.3% of the variance of 250-hPa zonal wind over the North Pacific and corresponds to longitudinal variability of the 250-hPa zonal wind in the vicinity of the exit region of the climatological NPJ. A positive EOF 1 pattern (+EOF 1) is associated with a zonal extension of the exit region of the climatological NPJ (i.e., a jet extension), while a negative EOF 1 pattern (–EOF 1) is associated with a retraction of the exit region of the climatological NPJ (i.e., a jet retraction). EOF 2 explains 7.8% of the variance of 250-hPa zonal wind over the North Pacific and corresponds to latitudinal variability of the 250-hPa zonal wind in the vicinity of the exit region of the climatological NPJ. A positive EOF 2 pattern (+EOF 2) is associated with a poleward shift of the exit region of the climatological NPJ (i.e., a poleward shift), while a negative EOF 2 pattern (–EOF 2) is associated with an equatorward shift of the exit region of the climatological NPJ (i.e., an equatorward shift). The combined variance explained by EOF 1 and EOF 2 is comparable to that found in previous studies (Athanasiadis et al. 2010; Jaffe et al. 2011; Griffin and Martin 2017) and the two leading EOFs are statistically well separated using the methodology outlined in North et al. (1982). To ensure that the EOF patterns shown in Fig. 1 are representative of the entire cool season, separate traditional EOF analyses were performed on three-month subsets of the 250-hPa zonal wind anomaly data. These independent EOF analyses (not shown) confirm that EOF 1 and EOF 2 represent the two leading modes of NPJ variability with fidelity throughout the cool season.

The magnitudes and signs of PC 1 and PC 2 are normalized to unit variance and time series constructed from the instantaneous PCs assist in characterizing the temporal evolution of the NPJ with respect to EOF 1 and EOF 2. As noted by Griffin and Martin (2017), the use of instantaneous PCs produces a noisy time series due to the high-frequency variability that characterizes the NPJ on daily time scales (their Fig. 1). Consequently, in an attempt to describe

203 the evolution of the NPJ with greater temporal coherence than the instantaneous PCs while
204 preserving the high-frequency variability of the NPJ on daily time scales, the instantaneous PCs
205 are smoothed through the calculation of a weighted average of the instantaneous PCs within ±24
206 h of each analysis time, t_0. The weight, w, prescribed to the instantaneous PCs at each analysis
207 time, t, within ±24 h of t_0 is defined as: $w = 5 - |t - t_0|/6$, for $|t - t_0| \leq 24$ h.
208 The weighted PCs at a particular analysis time can be plotted on a two-dimensional
209 Cartesian grid (i.e., the NPJ Phase Diagram) in an effort to visualize the state of the NPJ. The
210 position along the abscissa within the NPJ Phase Diagram corresponds to the value of weighted
211 PC 1 and indicates how strongly the 250-hPa zonal wind anomalies project onto EOF 1. Positive
212 and negative values of weighted PC 1 represent a jet extension and jet retraction, respectively.
213 The position along the ordinate within the NPJ Phase Diagram corresponds to the value of
214 weighted PC 2 and indicates how strongly the 250-hPa zonal wind anomalies project onto EOF
215 2. Positive and negative values of weighted PC 2 represent a poleward shift and equatorward
216 shift, respectively.
217 Examples of NPJ configurations that project strongly onto a jet extension and a jet
218 retraction regime are provided in Figs. 2a and 2b, respectively, while NPJ configurations that
219 project strongly onto a poleward shift and an equatorward shift regime are provided in Figs. 3a
220 and 3b, respectively. Considering these sample NPJ configurations, it is important to note that
221 the upper-tropospheric flow pattern at any one time is considerably more complex than that
222 implied by the NPJ Phase Diagram and the EOF patterns shown in Fig. 1. Nevertheless, given
223 that the NPJ Phase Diagram is constructed from the two leading modes of 250-hPa zonal wind
224 variability over the North Pacific during the cool season, plotting the weighted PCs on the NPJ
225 Phase Diagram and tracking their evolution over time encompasses many important aspects of

226 the NPJ and its evolution.

227 As for the sample cases shown in Figs. 2 and 3, the weighted PCs at all analysis times
228 during 1979–2014 excluding the summer months are plotted on the NPJ Phase Diagram in order
229 to classify each analysis time into one of the four NPJ regimes, or to identify analysis times
230 during which the NPJ lies within the unit circle (Fig. 4). For this classification scheme, the
231 analysis times are classified based on, first, whether the position of the NPJ within the NPJ Phase
232 Diagram is greater than a distance of 1 standard deviation from the origin and, second, whether
233 the absolute value of PC 1 or PC 2 is greater. Analysis times that fall into the "origin" category
234 are interpreted as times during which the NPJ exhibits a structure not far from climatology, or at
235 least a structure that does not project strongly onto EOF 1 and EOF 2. Plotting the weighted PCs
236 onto the NPJ Phase Diagram over a specified time interval yields a trajectory within the NPJ
237 Phase Diagram that describes the evolution of the NPJ.

238 **3. Characteristics of the NPJ Phase Diagram**

239 The classification of analysis times discussed in section 2 reveals several salient
240 characteristics of each NPJ regime. The number of analysis times characterized by each NPJ
241 regime and the typical residence time of the NPJ within each NPJ regime are provided in Table
242 1. Overall, the mean and median residence time within an NPJ regime do not vary considerably
243 between the NPJ regimes. Specifically, the mean residence time within an NPJ regime ranges
244 between 3.58 and 3.85 days, while the median residence time ranges between 2.50 and 2.75
245 days[3]. The residence time is slightly longer for periods during which the NPJ resides within 1
246 standard deviation of the origin in the NPJ Phase Diagram, with a mean and median residence
247 time of 4.65 and 3.25 days, respectively. The mean residence time is larger than the median for

[3] The mean and median residence times shown in Table 1 are sensitive to the smoothing procedure described in section 2. The use of instantaneous PCs yields mean and median residence times that are approximately a day shorter than those discussed in the text.

each NPJ regime, which highlights the degree to which the distribution of residence times is positively skewed towards a few persistent, long-lasting NPJ regimes. In support of this observation, an examination of the minimum and maximum residence time within each NPJ regime indicates that while an NPJ regime can be transient, it can also persist for multiple weeks.

As demonstrated from previous studies on NPJ variability, each NPJ regime exhibits a strong influence on the character of the downstream large-scale flow pattern over North America (e.g., Athanasiadis et al. 2010; Jaffe et al. 2011; Griffin and Martin 2017). To ensure consistency with previous studies, composite analyses are constructed employing the CFSR for periods during which the NPJ resided within the same NPJ regime for at least three consecutive days. A three-day threshold is chosen as a compromise between the magnitude of the mean and median residence time for each NPJ regime (Table 1). Figure 5 illustrates the characteristic large-scale flow pattern four days following the onset of each NPJ regime. A four-day time lag is chosen to highlight both the characteristic structure of the NPJ as well as the downstream flow pattern over North America associated with each NPJ regime. Two-sided Student's *t* tests were performed on the geopotential height and temperature anomaly fields shown in Fig. 5 to identify anomalies that are statistically distinct from climatology at the 99% confidence level.

A jet extension is characterized by the meridional juxtaposition of an anomalous upper-tropospheric trough over the central North Pacific and an anomalous ridge over the subtropical North Pacific that combine to produce a strong, zonally oriented NPJ (Fig. 5a). Beneath the left-exit region of the extended NPJ, an anomalous surface cyclone induces anomalous southerly geostrophic flow along the west coast of North America (Fig. 5b). This southerly geostrophic flow is collocated with lower-tropospheric warm anomalies over western North America as well as an anomalous upper-tropospheric ridge in the same location (Fig. 5a). Lower-tropospheric

cold anomalies are found upstream of the surface cyclone in association with anomalous northerly geostrophic flow over the central North Pacific, and across eastern North America beneath an anomalous upper-tropospheric trough (Fig. 5b).

A jet retraction features upper- and lower-tropospheric patterns that are largely opposite of those observed for a jet extension. In particular, a jet retraction is associated with an anomalous upper-tropospheric ridge over the central North Pacific, and anomalous troughs over northwestern North America and the subtropical North Pacific (Fig. 5c). In combination, these geopotential height anomalies result in a retracted NPJ to the west of the date line. Directly beneath the central North Pacific ridge, the circulation concomitant with an anomalous surface anticyclone is associated with lower-tropospheric cold anomalies over Alaska and the west coast of North America, and warm anomalies over the central North Pacific (Fig. 5d). Lower-tropospheric warm anomalies are also found in the south-central U.S. upstream of an anomalous upper-tropospheric ridge positioned over the southeastern U.S.

A poleward shift exhibits an anomalous upper-tropospheric trough over the high-latitude North Pacific and an anomalous ridge over the subtropical North Pacific that act in combination to position the exit region of the NPJ poleward of 40°N (Fig. 5e). An anomalous surface cyclone is located beneath the left-exit region of the poleward-shifted NPJ, which results in anomalous southerly geostrophic flow within an area characterized by lower-tropospheric warm anomalies over northern North America (Fig. 5f). These lower-tropospheric warm anomalies are also associated with an anomalous upper-tropospheric ridge positioned over eastern Canada (Fig. 5e). Lower-tropospheric cold anomalies are only observed over the Bering Strait and Gulf of Alaska during a poleward shift in conjunction with anomalous northerly geostrophic flow upstream of the surface cyclone (Fig. 5f).

294 An equatorward shift features upper- and lower-tropospheric flow patterns that are
295 largely opposite of those observed for a poleward shift. Specifically, an equatorward shift is
296 associated with an anomalous upper-tropospheric ridge over the high-latitude North Pacific and
297 an anomalous trough over the subtropical North Pacific (Fig. 5g), reminiscent of a Rex block
298 (Rex 1950). This configuration of geopotential height anomalies results in an equatorward
299 deflection of the exit region of the NPJ near the date line, and a weaker NPJ over the western
300 North Pacific compared to the other NPJ regimes. An anomalous upper-tropospheric trough is
301 also positioned over eastern Canada downstream of the high-latitude ridge over the North Pacific
302 (Fig. 5g). In the lower-troposphere, an equatorward shift is associated with an anomalous surface
303 anticyclone centered near the Aleutian Islands (Fig. 5h). This surface anticyclone induces
304 anomalous northerly geostrophic flow within an area characterized by lower-tropospheric cold
305 anomalies downstream of the surface anticyclone over northern North America. Conversely,
306 anomalous southerly geostrophic flow upstream of the surface anticyclone is associated with the
307 presence of lower-tropospheric warm anomalies over the Bering Strait and the Gulf of Alaska.
308 Consideration of the interannual and intraseasonal variability of each NPJ regime offers
309 insight into the characteristic structure of the NPJ. While the NPJ resides within one of the four
310 NPJ regimes (i.e., outside a radius of 1 standard deviation from the origin) 59% of the time
311 during an average cool season (not shown), there is considerable interannual variability in the
312 frequency of each NPJ regime (Fig. 6a). As an example, the 1997–1998 cool season was
313 characterized by the second-lowest annual frequency of poleward shifts (4.7%), while the
314 subsequent 1998–1999 cool season featured the highest annual frequency of poleward shifts
315 (34.9%). Comparable abrupt changes in the annual frequency of an individual NPJ regime are
316 readily observed when considering the time series for other NPJ regimes. Furthermore, linear

317 regressions performed on each of the time series shown in Fig. 6a do not identify any statistically
318 significant trends in the frequency of each NPJ regime during 1979–2014 (not shown).
319 There is considerable intraseasonal variability in the frequency of each NPJ regime, as
320 well (Fig. 6b). Specifically, the NPJ resides within an NPJ regime most frequently during
321 November–March and less frequently during the months of September, October, April, and May.
322 Both jet extensions and jet retractions peak in frequency during the month of March, while
323 poleward shifts and equatorward shifts peak during February and January, respectively. The
324 frequencies of each NPJ regime during an individual month are generally comparable, except
325 during March, when jet extensions and jet retractions are noticeably more frequent than poleward
326 shifts and equatorward shifts, and during September, when poleward shifts and equatorward
327 shifts are considerably more frequent than jet extensions and jet retractions.
328 As might be anticipated, the interannual and intraseasonal frequency of each NPJ regime
329 are related to large-scale atmospheric teleconnection patterns. For example, the Pacific–North
330 American (PNA) pattern is known to be strongly related to the intensity of the NPJ (e.g., Wallace
331 and Gutzler 1981; Barnston and Livesey 1987; Franzke and Feldstein 2005; Strong and Davis
332 2008; Athanasiadis et al. 2010; Wettstein and Wallace 2010; Franzke et al. 2011; Griffin and
333 Martin 2017). Specifically, a positive PNA pattern is characterized by an anomalous upper-
334 tropospheric trough over the central North Pacific and an anomalous ridge over the subtropical
335 North Pacific. Consequently, a positive PNA pattern is conducive to an extended (Fig. 5a) or
336 poleward-shifted NPJ (Fig. 5e). Conversely, a negative PNA pattern exhibits an anomalous
337 upper-tropospheric ridge over the central North Pacific, which favors a retracted (Fig. 5c) or
338 equatorward-shifted NPJ (Fig. 5g).
339 To illustrate the relationship between the PNA and each NPJ regime, all analysis times

that were characterized by an NPJ regime (i.e., outside a radius of 1 standard deviation from the origin) were classified based on the sign and magnitude of the daily PNA index (CPC 2017a). Analysis times that featured a PNA index > 0.5 (PNA index < –0.5) were classified as occurring during a positive (negative) PNA, and those remaining were classified as occurring during a neutral PNA. Figure 7a demonstrates that the frequency of each NPJ regime is well associated with the phase of the PNA. In particular, a positive PNA is most frequently characterized by jet extensions and poleward shifts, while a negative PNA is most frequently characterized by jet retractions and equatorward shifts.

The frequency of each NPJ regime also exhibits an association with the phase of the Arctic Oscillation (AO; e.g., Thompson and Wallace 1998; Higgins et al. 2000). The positive (negative) phase of the AO is characterized by above-normal (below-normal) 1000-hPa geopotential heights over the central North Pacific and below-normal (above-normal) 1000-hPa geopotential heights over the Arctic. As for the PNA index, daily AO indices (CPC 2017b) are employed to classify analysis times that were characterized by an NPJ regime. Analysis times exhibiting an AO index > 0.5 (AO index < –0.5) were classified as occurring during a positive (negative) AO, and those remaining were classified as occurring during a neutral AO. Figure 7b indicates that a positive AO is most frequently characterized by jet retractions and a negative AO is most frequently characterized by jet extensions. This relationship agrees with the NPJ regime composites shown in Figs. 5d and 5b, given that jet retractions are associated with an anomalous surface anticyclone over the central North Pacific (Fig. 5d), and jet extensions feature an anomalous surface cyclone in that location (Fig. 5b).

The structure of the NPJ is also related to the El Niño–Southern Oscillation (ENSO). For example, prior work suggests that anomalous convection and above-normal sea surface

363 temperatures over the central and eastern equatorial Pacific during an El Niño favor an extended
364 or equatorward-shifted NPJ. Conversely, anomalous convection and above-normal sea-surface
365 temperatures over the western equatorial Pacific during a La Niña favor a retracted or poleward-
366 shifted NPJ (e.g., Horel and Wallace 1981; Rasmusson and Wallace 1983; Rasmusson and Mo
367 1993; Yang et al. 2002; Li and Wettstein 2012; Xie et al. 2015; Cook et al. 2017). In an effort to
368 frame this relationship with respect to the NPJ Phase Diagram, analysis times that were
369 characterized by an NPJ regime were classified based on the sign and magnitude of the monthly
370 Niño-3.4 index (ESRL 2017). Analysis times that coincided with a Niño-3.4 index > 1.0 (Niño-
371 3.4 index < –1.0) were classified as occurring during an El Niño (a La Niña), and those
372 remaining were classified as occurring during a neutral ENSO state. Figure 7c demonstrates that
373 El Niño is most frequently characterized by jet extensions and equatorward shifts. Conversely,
374 La Niña is most frequently characterized by jet retractions and poleward shifts. The results from
375 Fig. 7c translate to individual cool seasons characterized by El Niño and La Niña events, as well.
376 For example, Fig. 6a indicates that the 1982–1983 El Niño cool season (Sep–May Niño 3.4 =
377 1.82) was most frequently characterized by jet extensions and equatorward shifts, while the
378 1999–2000 La Niña cool season (Sep–May Niño 3.4 = –1.22) was most frequently characterized
379 by jet retractions and poleward shifts.

380 **4. GEFS forecast skill with respect to the NPJ Phase Diagram**

381 Given the relationship between each NPJ regime and the downstream large-scale flow
382 pattern over North America (Fig. 5), additional knowledge of the forecast skill associated with
383 each NPJ regime offers the potential to increase confidence in operational medium-range
384 forecasts over North America. To evaluate the forecast skill associated with each NPJ regime, an
385 ensemble of 9-day forecast trajectories within the NPJ Phase Diagram are calculated daily during

386 1985–2014 excluding the summer months using 250-hPa zonal wind data from the 1.0°-
387 resolution[4] GEFS Reforecast Version 2 dataset (Hamill et al. 2013). The GEFS Reforecast
388 dataset features 10 ensemble member forecasts and 1 control member forecast initialized daily at
389 0000 UTC, each with forecast lead times as long as 384 h.

390 Forecast errors are defined with respect to NPJ Phase Diagram and are calculated as the
391 Euclidean distance error in standard deviations between the ensemble mean NPJ Phase Diagram
392 forecast and the verifying 0-h analysis that corresponds to each forecast lead time. The NPJ
393 Phase Diagram forecasts are then classified based on (1) the position of the NPJ within the NPJ
394 Phase Diagram at the time of forecast initialization or forecast verification according to the
395 schematic shown in Fig. 4 and (2) season. Two-sided Student's *t* tests are performed on all NPJ
396 Phase Diagram forecast error statistics to assess statistical significance in accordance with the
397 specifications described in each pertinent figure caption. Recall from section 2 that the upper-
398 tropospheric flow pattern is considerably more complex than that implied by the NPJ Phase
399 Diagram. Consequently, the forecast error metric employed in the present study only describes a
400 fraction of the total forecast error insofar as it relates to the position and intensity of the NPJ.

401 The average distance errors associated with ensemble mean NPJ Phase Diagram forecasts
402 initialized during the same season are provided in Fig. 8a. The average distance errors are
403 displayed here, and in subsequent figure panels, as an average percent error relative to the
404 average distance error of all ensemble mean NPJ Phase Diagram forecasts for each lead time. For
405 example, average percent errors greater than (less than) zero indicate that forecasts within a
406 particular category are associated with an average distance error that is greater than (less than)
407 that associated with all ensemble mean NPJ Phase Diagram forecasts at a certain lead time. At

[4] While the GEFS Reforecast Version 2 dataset is available at 1.0° resolution, the GEFS was run at a resolution of ~0.5° for week 1 reforecasts and a resolution of ~0.75° for week 2 reforecasts (Hamill et al. 2013).

lead times ≤ 120 h, NPJ Phase Diagram forecasts initialized during the winter (Dec–Feb) exhibit significantly larger distance errors within the NPJ Phase Diagram than forecasts initialized during the fall (Sep–Nov) and spring (Mar–May). At lead times ≥ 168 h, forecasts initialized during the winter and spring exhibit significantly larger distance errors than forecasts initialized during the fall. Furthermore, forecasts initialized during the fall exhibit distance errors that fall below the cool-season average at all forecast lead times, while forecasts initialized during the winter exhibit errors that lie above the cool-season average at all forecast lead times.

The average distance errors of ensemble mean NPJ Phase Diagram forecasts initialized during the same NPJ regime are shown in Fig. 8b. At lead times < 120 h, no significant differences in distance error are observed between the NPJ regimes. However, significant differences between the NPJ regimes begin to emerge at lead times ≥ 120 h. Specifically, forecasts initialized during a jet retraction exhibit significantly larger distance errors than forecasts initialized during a poleward shift at lead times between 120 h and 168 h, and significantly larger distance errors than forecasts initialized during a jet extension at lead times between 192 h and 216 h. However, despite these significant differences at lead times ≥ 120 h, the spread in distance errors between the NPJ regimes is generally small during this time period.

The average distance errors of ensemble mean NPJ Phase Diagram forecasts verified during the same NPJ regime are shown in Fig. 8c. At lead times ≥ 144 h, forecasts verified during equatorward shifts and jet retractions exhibit significantly larger distance errors than those verified during poleward shifts and jet extensions. Additionally, considerably larger spread between the distance errors associated with each NPJ regime is observed for NPJ Phase Diagram forecasts verified during the same NPJ regime (Fig. 8c) compared to those initialized during the same NPJ regime (Fig. 8b) for this time period. Consequently, knowledge of the NPJ regime at

431 the time of forecast verification appears to be a greater differentiator of forecast skill with respect
432 to the NPJ Phase Diagram than knowledge of the NPJ regime at the time of forecast
433 initialization. This result implies that enhanced or reduced confidence can be ascribed to a
434 forecast by considering the forecast evolution of the NPJ with respect to the NPJ Phase Diagram,
435 rather than by considering the state of the NPJ at the time of forecast initialization.

436 The poor forecast skill of ensemble mean NPJ Phase Diagram forecasts verified during
437 equatorward shifts (Fig. 8c) is also apparent when considering the frequency with which each
438 NPJ regime is overforecast or underforecast in the GEFS Reforecast dataset. Figure 9
439 demonstrates that equatorward shifts are substantially underforecast by ensemble mean NPJ
440 Phase Diagram forecasts at all lead times compared to the verifying 0-h analyses. Specifically,
441 equatorward shifts are underforecast by nearly 26% at a 216-h lead time, which is at least twice
442 the frequency that the other NPJ regimes are underforecast at the same lead time. While all NPJ
443 regimes are generally underforecast by the ensemble mean NPJ Phase Diagram forecasts at lead
444 times $\geq$ 192 h, both jet extensions and poleward shifts are overforecast at lead times $\leq$ 144 h. The
445 overforecasting of NPJ regimes near the origin of the NPJ Phase Diagram suggests a general
446 reversion of the ensemble mean 250-hPa zonal wind towards climatology for long forecast lead
447 times.

448 **5. Best and worst NPJ Phase Diagram forecasts**

449 An examination of the best and worst NPJ Phase Diagram medium-range forecasts has
450 the potential to illuminate factors that may contribute to enhanced or reduced forecast skill
451 during the medium-range period (e.g., Lillo and Parsons 2017). The best and worst medium-
452 range forecasts with respect to the NPJ Phase Diagram are identified in terms of the following
453 two metrics: (1) the magnitude of the GEFS ensemble mean distance error averaged over lead

454 times of 192 h and 216 h, and (2) the magnitude of the GEFS ensemble member distance error
455 averaged over all ensemble members at lead times of 192 h and 216 h. The first metric provides
456 a measure of ensemble-mean forecast accuracy during the medium-range period, while the
457 second metric provides a measure of ensemble-member forecast precision. Those forecasts that
458 rank in the top 10% in terms of the average ensemble mean distance error *and* the top 10% in
459 terms of the average ensemble member distance error are identified as best forecasts.
460 Conversely, those forecasts that rank in the bottom 10% in terms of both metrics (i.e., the largest
461 average distance errors) are identified as worst forecasts.

462 Figure 10 describes a series of hypothetical NPJ Phase Diagram forecasts that qualify
463 either as a best, an intermediate, or a worst forecast with respect to the two metrics identified in
464 the previous paragraph. A best forecast (Fig. 10a) is one in which the forecast exhibits a small
465 average ensemble mean distance error and a small average ensemble member distance error.
466 Therefore, a best forecast is interpreted as one in which the forecast is both accurate and precise.
467 An intermediate forecast (Fig. 10b) is one in which there is a small average ensemble mean
468 distance error but also a large average ensemble member distance error. Consequently, the
469 criteria for a best forecast is not met and this situation represents one in which the forecast was
470 accurate but not precise. A worst forecast is one in which there is a large average ensemble mean
471 distance error and a large average ensemble member distance error. Such a forecast can either be
472 inaccurate but precise (Fig. 10c), or inaccurate and not precise (Fig. 10d). Considered together,
473 the worst forecasts can be summarized as those forecasts that feature the highest degree of
474 inaccuracy.

475 The frequency distribution of the worst NPJ Phase Diagram forecasts during the cool
476 season features two separate maxima during December and during February–April, while the

best NPJ Phase Diagram forecasts occur most frequently during September (Fig. 11a). The best and worst NPJ Phase Diagram forecasts are classified based on the NPJ regime at the time of forecast initialization in Fig. 11b. This frequency distribution indicates that the worst forecasts are initialized disproportionately more than the best forecasts during jet retractions and equatorward shifts, while the best forecasts are initialized disproportionately more than the worst forecasts during jet extensions and poleward shifts. The average value of PC 1 and PC 2 at the time of forecast initialization (Table 2) also indicates a preference for the worst forecasts to be initialized most frequently during jet retractions and equatorward shifts, and for the best forecasts to be initialized most frequently during jet extensions and poleward shifts. However, only the values of PC 1 are significantly different between the best and worst forecasts at the time of forecast initialization.

The evolution of the NPJ during the 10-day period following the initialization of a best and worst NPJ Phase Diagram forecast also differs considerably (Table 2). In particular, the average change in PC 2 (ΔPC 2) during the 10-day period following the initialization of a worst forecast indicates a significant movement of the NPJ towards an equatorward shift within the NPJ Phase Diagram, while the ΔPC 2 following the initialization of a best forecast indicates a significant movement of the NPJ towards a poleward shift. Additionally, the worst forecast periods feature significantly longer trajectories within the NPJ Phase Diagram compared to the best forecast periods during the 10-day period following forecast initialization (Table 2). As will be demonstrated, this result is consistent with the notion that the worst forecasts often occur during periods characterized by rapid NPJ regime change, while the best forecast periods are often characterized by more persistent upper-tropospheric flow patterns over the North Pacific in comparison. This notion aligns well with previous work suggesting that periods characterized by

500 upper-tropospheric regime change are generally associated with reduced forecast skill (e.g.,
501 Tibaldi and Molteni 1990; Frederiksen et al. 2004; Pelly and Hoskins 2006; Ferranti et al. 2015;
502 Lillo and Parsons 2017).

503 An examination of the upper-tropospheric flow patterns associated with the best and
504 worst forecast periods offers insight into the types of large-scale flow patterns that are
505 characterized by enhanced or reduced forecast skill. This examination is performed by
506 employing the CFSR to construct composite analyses of 250-hPa wind speed, geopotential
507 height, and geopotential height anomalies at the time a best and worst forecast are initialized, as
508 well as at 192 h following forecast initialization. Two-sided Student's *t* tests are used to evaluate
509 whether the differences between geopotential height anomalies associated with the worst and
510 best forecast composites are statistically significant at the 99% confidence level at each time
511 period.

512 The composite upper-tropospheric flow patterns at the time a best and worst forecast are
513 initialized within each NPJ regime are provided in Fig. 12. At first glance, an examination of the
514 geopotential height anomalies in Fig. 12 reveals minor qualitative differences between the best
515 and worst forecasts that are initialized during the same NPJ regime. However, a calculation of
516 the difference between geopotential height anomalies associated with the worst and best
517 forecasts reveals some significant features (Fig. 13). In particular, while both the best and worst
518 forecasts that are initialized during a jet extension exhibit a strong, zonally extended NPJ at the
519 time of forecast initialization (Figs. 12a,b), the worst forecasts are characterized by significantly
520 higher geopotential height anomalies over the eastern North Pacific compared to the best
521 forecasts (Fig. 13a). Similarly, while both the best and worst forecasts that are initialized during
522 a jet retraction feature an anomalous ridge over the central North Pacific (Figs. 12c,d), the worst

forecasts also exhibit significantly higher geopotential height anomalies over the eastern North Pacific compared to the best forecasts (Fig. 13b). The worst forecasts that are initialized during a jet retraction also feature significantly lower geopotential height anomalies over the subtropical North Pacific and the western Great Lakes compared to the best forecasts (Fig. 13b).

Similar to jet extensions and jet retractions, the worst forecasts that are initialized during a poleward shift exhibit significantly higher geopotential height anomalies over the eastern North Pacific compared to the best forecasts (Figs. 12e,f and 13c). Furthermore, the worst forecasts that are initialized during a poleward shift feature a more intense NPJ, a stronger jet stream over North America, and significantly lower geopotential height anomalies over the southwestern U.S. and northwestern Mexico compared to the best forecasts (Figs. 12e,f and 13c). While not as large in magnitude compared to the other composites, the worst forecasts that are initialized during an equatorward shift also exhibit significantly higher geopotential height anomalies over the eastern North Pacific compared to the best forecasts (Figs. 12g,h and 13d). Consequently, the presence of higher geopotential height anomalies over the eastern North Pacific at the time of forecast initialization is a distinguishing factor between the worst and best forecasts regardless of the prevailing NPJ regime.

Substantial differences in the upper-tropospheric flow pattern over the North Pacific are observed 192 h following the initialization of a best and worst forecast. In particular, the upper-tropospheric flow pattern 192 h following the initialization of a best forecast is characterized by the meridional juxtaposition of an anomalous trough and an anomalous ridge over the central North Pacific regardless of the NPJ regime at the time of forecast initialization (Figs. 14a,c,e,g). This pattern subsequently favors an NPJ that is extended and poleward-shifted in the best forecast composites relative to the worst forecast composites. Downstream of the anomalous

546 trough over the North Pacific, an anomalous ridge is also firmly positioned over North America
547 in the best forecast composites. In contrast to the best forecasts, the upper-tropospheric flow
548 pattern 192 h following the initialization of a worst forecast features an anomalous ridge over the
549 high-latitude North Pacific and a retracted NPJ regardless of the NPJ regime at the time of
550 forecast initialization (Figs. 14b,d,f,h). An anomalous trough of variable strength is also located
551 over North America in all of the worst forecast composites.

552 The difference between the geopotential height anomalies 192 h following the
553 initialization of a worst and best forecast is shown in Fig. 15. Compared to the best forecast
554 composites, all of worst forecast composites exhibit significantly higher geopotential height
555 anomalies over the high-latitude North Pacific, and significantly lower geopotential height
556 anomalies over the subtropical North Pacific (Figs. 15a–d), reminiscent of a Rex block (Rex
557 1950). Notably, this difference pattern prevails regardless of the NPJ regime at the time of
558 forecast initialization. Consequently, the upper-tropospheric flow patterns shown in Fig. 15
559 uniformly suggest that periods characterized by the development and/or maintenance of upper-
560 tropospheric blocking events over the North Pacific are associated with reduced forecast skill
561 with respect to the NPJ Phase Diagram. Conversely, reversing the sign of the difference field in
562 Fig. 15 (not shown) suggests that periods evolving towards a zonal NPJ over the North Pacific
563 are generally associated with enhanced forecast skill.

564 **6. Discussion and conclusions**

565 The preceding analysis corroborates the results from prior studies on NPJ variability that
566 establish a relationship between the two leading modes of 250-hPa zonal wind variability over
567 the North Pacific and the large-scale flow pattern over North America (e.g., Athanasiadis et al.
568 2010; Jaffe et al. 2011; Griffin and Martin 2017). Provided with this relationship, this study

569 utilizes the two leading modes of 250-hPa zonal wind variability within the CFSR during the
570 cool season as the foundation for developing an NPJ Phase Diagram. The NPJ Phase Diagram
571 subsequently provides an objective tool to monitor the state and evolution of the upper-
572 tropospheric flow pattern over the North Pacific, to identify the prevailing NPJ regime, and to
573 evaluate the characteristic forecast skill associated with each NPJ regime.

574 The application of the NPJ Phase Diagram to 250-hPa zonal wind data from the CFSR
575 during 1979–2014 excluding the summer months reveals several salient characteristics of each
576 NPJ regime and highlights opportunities for additional research. For example, while the mean
577 and median residence times within a particular NPJ regime are typically on the order of three
578 days, an NPJ regime can persist for multiple weeks. Furthermore, it is apparent that the
579 frequency of each NPJ regime is characterized by considerable interannual and intraseasonal
580 variability. Given that each NPJ regime can strongly influence the character of the downstream
581 flow pattern over North America, further investigation into the types of large-scale flow patterns
582 that are conducive to prolonged residence times within an NPJ regime, or that increase the
583 frequency of an NPJ regime, may add considerable value to operational seasonal and subseasonal
584 forecasts over North America.

585 Large-scale atmospheric teleconnection patterns, such as the PNA, AO, and ENSO, are
586 strongly related to frequency of each NPJ regime. For example, it was noted that a positive
587 (negative) PNA is most frequently characterized by jet extensions and poleward shifts (jet
588 retractions and equatorward shifts). Jet extensions and poleward shifts are associated with
589 different lower-tropospheric temperature anomaly patterns over North America, however, with
590 jet extensions favoring anomalously cold temperatures over eastern North America and poleward
591 shifts favoring anomalously warm temperatures over northern North America. Consequently,

knowledge of the prevailing NPJ regime in combination with the phase of the PNA index provides additional value to operational forecasts of temperature over North America.

The NPJ Phase Diagram provides an objective basis for detailed investigations of NPJ variability during other well-established atmospheric teleconnection patterns, as well, such as the North Atlantic Oscillation (e.g., Wallace and Gutzler 1981) and the Madden–Julian Oscillation (Madden and Julian 1972). Such investigations have the potential to identify the variety of large-scale flow evolutions over the North Pacific that occur during a particular atmospheric teleconnection pattern. Similar to the approach utilized by Madonna et al. (2017) in their investigation of North Atlantic jet variability, cluster analysis techniques can also be applied to 250-hPa zonal wind data to identify recurring non-linear configurations of the NPJ. These recurring non-linear configurations of the NPJ can be subsequently paired with the results from the present study to provide a complementary perspective on NPJ variability.

An examination of the forecast skill associated with each NPJ regime reveals the types of large-scale flow patterns that exhibit reduced forecast skill with respect to the NPJ Phase Diagram. In particular, the analysis suggests that forecasts verified during jet retractions and equatorward shifts exhibit significantly reduced forecast skill compared to jet extensions and poleward shifts at lead times $\geq$ 144 h. Recall that both jet retractions and equatorward shifts are typically characterized by an anomalous upper-tropospheric ridge in the central North Pacific. In light of these two observations, and given that diabatic processes can play an important role in amplifying the upper-tropospheric flow pattern (e.g., Massacand et al. 2001; Riemer et al. 2008; Torn 2010; Ferranti et al. 2015; Pfahl et al. 2015; Grams and Archambault 2016; Bosart et al. 2017), it is hypothesized that diabatic processes account for a considerable fraction of the reduced forecast skill associated with jet retractions and equatorward shifts. Additional case

615 study work that utilizes the NPJ Phase Diagram to investigate poor forecasts verified during jet
616 retractions and equatorward shifts is likely to determine the degree to which diabatic processes
617 contribute to the reduced forecast skill associated with these NPJ regimes.

618 An analysis of the best and worst medium-range forecasts with respect to the NPJ Phase
619 Diagram suggests that the worst forecasts are often associated with the development and/or
620 maintenance of upper-tropospheric blocking events over the North Pacific. This result aligns
621 well with previous work highlighting the reduced predictability associated with the development
622 and/or maintenance of blocking events (e.g., Tibaldi and Molteni 1990; D'Andrea et al. 1998;
623 Frederiksen et al. 2004; Pelly and Hoskins 2006; Matsueda 2011; Ferranti et al. 2015) and holds
624 regardless of the prevailing NPJ regime at the time of forecast initialization. Given this
625 variability in the prevailing NPJ regime prior to blocking events, additional work is required to
626 determine the types of large-scale flow evolutions that are most conducive to block development.
627 The NPJ Phase Diagram is well suited for such work by providing an objective frame of
628 reference from which to examine the spectrum of large-scale flow evolutions that are conducive
629 to block development. The analysis also indicates that the worst forecast periods are associated
630 with a significant movement of the NPJ towards an equatorward shift within the NPJ Phase
631 Diagram during the 10-day period following forecast initialization, while the best forecast
632 periods are associated with a significant movement of the NPJ towards a poleward shift. Given
633 that certain trajectories within the NPJ Phase Diagram are associated with reduced forecast skill,
634 the NPJ Phase Diagram represents a tool that can be used to objectively identify NPJ regime
635 transitions and to isolate the characteristic large-scale flow patterns associated with those regime
636 transitions. The results from such an investigation have the potential to add considerable value to
637 operational forecasts during periods of regime transition.

638 The relative forecast skill associated with each NPJ regime is only applicable with
639 respect to the GEFS Reforecast dataset in the present study. Consequently, additional research is
640 required to evaluate the forecast skill of NPJ regimes with respect to other ensemble prediction
641 systems (EPSs). An evaluation of forecast skill with respect to other EPSs has the potential to
642 determine whether the large-scale flow patterns that exhibit reduced skill in the GEFS Reforecast
643 dataset differ from those that exhibit reduced skill in other EPSs. To the degree that differences
644 exist in the forecast skill of each NPJ regime across EPSs, such an evaluation has the potential to
645 identify situations during which greater confidence can be ascribed to a particular EPS and to
646 identify systematic biases in the evolution of certain large-scale flow patterns over the North
647 Pacific.
648
649 *Acknowledgments*
650 The authors thank Mike Bodner, Daniel Halperin, Arlene Laing, Bill Lamberson, Sara Ganetis,
651 and Josh Kastman for their constructive discussions concerning the NPJ Phase Diagram. The
652 authors also thank three anonymous reviewers for their constructive comments on this work and
653 the National Oceanic and Atmospheric Administration for its support of this work via Grant
654 NA15NWS4680006.

655 REFERENCES

656 Archambault, H. M., L. F. Bosart, D. Keyser, and J. M. Cordeira, 2013: A climatological
657 analysis of the extratropical flow response to recurving western North Pacific tropical
658 cyclones. *Mon. Wea. Rev.*, **141**, 2325–2346, doi: 10.1175/MWR-D-12-00257.1.

659 Archambault, H. M., D. Keyser, L. F. Bosart, C. A. Davis, and J. M. Cordeira, 2015: A
660 composite perspective of the extratropical flow response to recurving western North
661 Pacific tropical cyclones. *Mon. Wea. Rev.*, **143**, 1122–1141, doi: 10.1175/MWR-D-14-
662 00270.1.

663 Athanasiadis, P. J., J. M. Wallace, and J. J. Wettstein, 2010: Patterns of wintertime jet stream
664 variability and their relation to the storm tracks. *J. Atmos. Sci.*, **67**, 1361–1381, doi:
665 10.1175/2009JAS3270.1.

666 Barnston, A. G., and R. E. Livezey, 1987: Classification, seasonality and persistence of low-
667 frequency atmospheric circulation patterns. *Mon. Wea. Rev.*, **115**, 1083–1126, doi:
668 10.1175/1520-0493(1987)115<1083:CSAPOL>2.0.CO;2.

669 Bosart, L. F., B. J. Moore, J. M. Cordeira, and H. M. Archambault, 2017: Interactions of North
670 Pacific tropical, midlatitude, and polar disturbances resulting in linked extreme weather
671 events over North America in October 2007. *Mon. Wea. Rev.*, **145**, 1245–1273, doi:
672 10.1175/MWR-D-16-0230.1.

673 Chang, E. K. M., S. Lee, and K. L. Swanson, 2002: Storm track dynamics. *J. Climate*, **15**, 2163–
674 2183, doi: 10.1175/1520-0442(2002)015<02163:STD>2.0.CO;2.

675 Cook, A. R., L. M. Leslie, D. B. Parsons, and J. T. Schaefer, 2017: The impact of El Niño–
676 Southern Oscillation (ENSO) on winter and early spring U.S. tornado outbreaks. *J. Appl.*
677 *Meteor. Climatol.*, **56**, 2455–2478, doi: 10.1175/JAMC-D-16-0249.1.

CPC, 2017a: Pacific/North American pattern. Accessed 9 February 2017, http://www.cpc.ncep.noaa.gov/products/precip/CWlink/pna/pna.shtml.

CPC, 2017b: Arctic Oscillation. Accessed 9 February 2017, http://www.cpc.ncep.noaa.gov/products/precip/CWlink/daily_ao_index/ao.shtml.

D'Andrea, F., and Coauthors, 1998: Northern Hemisphere atmospheric blocking as simulated by 15 atmospheric general circulation models in the period 1979–1988. *Climate Dyn.*, **14**, 385–407, doi: 10.1007/s003820050230.

Eichelberger, S. J., and D. L. Hartmann, 2007: Zonal jet structure and the leading mode of variability. *J. Climate*, **20**, 5149–5163, doi: 10.1175/JCLI4279.1.

ESRL, 2017: Niño 3.4 SST Index. Accessed 5 January 2017, https://www.esrl.noaa.gov/psd/gcos_wgsp/Timeseries/Nino34/.

Ferranti, L., S. Corti, and M. Janousek, 2015: Flow-dependent verification of the ECMWF ensemble over the Euro-Atlantic sector. *Quart. J. Roy. Meteor. Soc.*, **141**, 916–924, doi: 10.1002/qj.2411.

Franzke, C., and S. B. Feldstein, 2005: The continuum and dynamics of Northern Hemisphere teleconnection patterns. *J. Atmos. Sci.*, **62**, 3250–3267, doi: 10.1175/JAS3536.1.

Franzke, C., S. B. Feldstein, and S. Lee, 2011: Synoptic analysis of the Pacific–North American teleconnection pattern. *Quart. J. Roy. Meteor. Soc.*, **137**, 329–346, doi: https://doi.org/10.1002/qj.768.

Frederiksen, J. S., M. A. Collier, and A. B. Watkins, 2004: Ensemble prediction of blocking regime transitions. *Tellus*, **56A**, 485–500, doi: 10.1111/j.1600-0870.2004.00075.x.

Grams, C. M., and H. M. Archambault, 2016: The key role of diabatic outflow in amplifying the midlatitude flow: A representative case study of weather systems surrounding western

North Pacific extratropical transition. *Mon. Wea. Rev.*, **144**, 3847–3869, doi: 10.1175/MWR-D-15-0419.1.

Griffin, K. S., and J. E. Martin, 2017: Synoptic features associated with temporally coherent modes of variability of the North Pacific jet stream. *J. Climate*, **30**, 39–54, doi: 10.1175/JCLI-D-15-0833.1.

Hakim, G. J., 2003: Developing wave packets in the North Pacific storm track. *Mon. Wea. Rev.*, **131**, 2824–2837, doi: 10.1175/1520-0493(2003)131<2824:DWPITN>2.0.CO;2.

Harr, P. A., and J. M. Dea, 2009: Downstream development associated with the extratropical transition of tropical cyclones over the western North Pacific. *Mon. Wea. Rev.*, **137**, 1295–1319, doi: 10.1175/2008MWR2558.1.

Hamill, T. M., G. T. Bates, J. S. Whitaker, D. R. Murray, M. Fiorino, T. J. Galarneau Jr., Y. Zhu, and W. Lapenta, 2013: NOAA's second-generation global medium-range ensemble reforecast dataset. *Bull. Amer. Meteor. Soc.*, **94**, 1553–1565, doi: 10.1175/BAMS-D-12-00014.1.

Handlos, Z. J., and J. E. Martin, 2016: Composite analysis of large-scale environments conducive to western Pacific polar/subtropical jet superposition. *J. Climate*, **29**, 7145–7165, doi: 10.1175/JCLI-D-16-0044.1.

Higgins, R. W., J.-K. E. Schemm, W. Shi, and A. Leetmaa, 2000: Extreme precipitation events in the western United States related to tropical forcing. *J. Climate*, **13**, 793–820, doi: 10.1175/1520-0442(2000)013<0793:EPEITW>2.0.CO;2.

Horel, J. D., and J. M. Wallace, 1981: Planetary-scale atmospheric phenomena associated with the Southern Oscillation. *Mon. Wea. Rev.*, **109**, 813–829, doi: 10.1175/1520-0493(1981)109<0813:PSAPAW>2.0.CO;2.

724 Hoskins, B. J., and D. J. Karoly, 1981: The steady linear response of a spherical atmosphere to
725 thermal and orographic forcing. *J. Atmos. Sci.*, **38**, 1179–1196, doi: 10.1175/1520-
726 0469(1981)038<1179:TSLROA>2.0.CO;2.
727 Jaffe, S. C., J. E. Martin, D. J. Vimont, and D. J. Lorenz, 2011: A synoptic climatology of
728 episodic, subseasonal retractions of the Pacific jet. *J. Climate*, **24**, 2846–2860, doi:
729 10.1175/2010JCLI3995.1.
730 Jhun, J.-G., and E.-J. Lee, 2004: A new East Asian winter monsoon index and associated
731 characteristics of the winter monsoon. *J. Climate*, **17**, 711–726, doi: 10.1175/1520-
732 0442(2004)017<0711:ANEAWM>2.0.CO;2.
733 Kalnay, E., and Coauthors, 1996: The NCEP/NCAR 40-year reanalysis project. *Bull. Amer.*
734 *Meteor. Soc.*, **77**, 437–471, doi: 10.1175/1520-0477(1996)077<0437:TNYRP>2.0.CO;2.
735 Lee, Y.-Y., G.-H. Lim, and J.-S. Kug, 2010: Influence of the East Asian winter monsoon on the
736 storm track activity over the North Pacific. *J. Geophys. Res.*, **115**, D09102, doi:
737 10.1029/2009JD012813.
738 Li, C., and J. J. Wettstein, 2012: Thermally driven and eddy-driven jet variability in reanalysis. *J.*
739 *Climate*, **25**, 1587–1596, doi: 10.1175/JCLI-D-11-00145.1.
740 Lillo, S. P., and D. B. Parsons, 2017: Investigating the dynamics of error growth in ECMWF
741 medium-range forecast busts. *Quart. J. Roy. Meteor. Soc.*, **143**, 1211–1226, doi:
742 10.1002/qj.2938.
743 Lin, H., and J. Derome, 1996: Changes in predictability associated with the PNA pattern. *Tellus*,
744 **48A**, 553–571, doi: 10.1034/j.1600-0870.1996.t01-3-00005.x.

745 Madden, R. A., and P. R. Julian, 1972: Description of global-scale circulation cells in the tropics
746 with a 40–50 day period. *J. Atmos. Sci.*, **29**, 1109–1123, doi: 10.1175/1520-
747 0469(1972)029<1109:DOGSCC>2.0.CO;2.
748 Madden, R. A., and P. R. Julian, 1994: Observations of the 40–50-day tropical oscillation—A
749 review. *Mon. Wea. Rev.*, **122**, 814–837, doi: 10.1175/1520-
750 0493(1994)122<0814:OOTDTO>2.0.CO;2.
751 Madonna, E., C. Li, C. M. Grams, and T. Woollings, 2017: The link between eddy-driven jet
752 variability and weather regimes in the North Atlantic-European sector. *Quart. J. Roy.*
753 *Meteor. Soc.*, **143**, 2960–2972, doi: 10.1002/qj.3155.
754 Massacand, A. C., H. Wernli, and H. C. Davies, 2001: Influence of upstream diabatic heating
755 upon an alpine event of heavy precipitation. *Mon. Wea. Rev.*, **129**, 2822–2828, doi:
756 10.1175/1520-0493(2001)129<2822:IOUDHU>2.0.CO;2.
757 Matsueda, M., 2011: Predictability of Euro-Russian blocking in summer of 2010. *Geophys. Res.*
758 *Lett.*, **38**, L06801, doi: 10.1029/2010GL046557.
759 North, G. R., T. L. Bell, R. F. Cahalan, and F. J. Moeng, 1982: Sampling errors in the estimation
760 of empirical orthogonal functions. *Mon. Wea. Rev.*, **110**, 699–706, doi: 10.1175/1520-
761 0493(1982)110<0699:SEITEO>2.0.CO;2.
762 Orlanski, I., and J. P. Sheldon, 1995: Stages in the energetics of baroclinic systems. *Tellus*, **47A**,
763 605–628, doi: 10.1034/j.1600-0870.1995.00108.x.
764 Palmer, T. N., 1988: Medium and extended range predictability and stability of the Pacific/North
765 American mode. *Quart. J. Roy. Meteor. Soc.*, **114**, 691–713. doi:
766 10.1002/qj.49711448108.

767 Pelly J. L., and B. J. Hoskins, 2006: How well does the ECMWF Ensemble Prediction System
768 predict blocking? *Quart. J. Roy. Meteor. Soc*., **129**, 1683–1702, doi: 10.1256/qj.01.173.
769 Pfahl, S., C. Schwierz, M. Croci-Maspoli, C. M. Grams, and H. Wernli, 2015: Importance of
770 latent heat release in ascending air streams for atmospheric blocking. *Nat. Geosci.*, **8**,
771 610–614, doi: 10.1038/ngeo2487.
772 Rasmusson, E. M., and J. M. Wallace, 1983: Meteorological aspects of the El Niño/Southern
773 Oscillation. *Science*, **222**, 1195–1202, doi: 10.1126/science.222.4629.1195.
774 Rasmusson, E. M., and K. Mo, 1993: Linkages between 200-mb tropical and extratropical
775 circulation anomalies during the 1986–1989 ENSO cycle. *J. Climate*, **6**, 595–616, doi:
776 10.1175/1520-0442(1993)006<0595:LBMTAE>2.0.CO;2.
777 Rex, D. F., 1950: Blocking action in the middle troposphere and its effect upon regional climate.
778 I: An aerological study of blocking action. *Tellus*, **2A**, 196–211, doi: 10.1111/j.2153-
779 3490.1950.tb00331.x.
780 Riemer, M., S. C. Jones, and C. A. Davis, 2008: The impact of extratropical transition on the
781 downstream flow: An idealized modelling study with a straight jet. *Quart. J. Roy.*
782 *Meteor. Soc.*, **134**, 69–91, doi: 10.1002/qj.189.
783 Saha, S., and Coauthors, 2010: The NCEP Climate Forecast System Reanalysis. *Bull. Amer.*
784 *Meteor. Soc.*, **91**, 1015–1057, doi: 10.1175/2010BAMS3001.1.
785 Saha, S., and Coauthors, 2014: The NCEP Climate Forecast System version 2. *J. Climate*, **27**,
786 2185–2208, doi: 10.1175/JCLI-D-12-00823.1.
787 Schubert, S. D., and C.-K. Park, 1991: Low-frequency intraseasonal tropical–extratropical
788 interactions. *J. Atmos. Sci.*, **48**, 629–650, doi: 10.1175/1520-
789 0469(1991)048<0629:LFITEI>2.0.CO;2.

790 Sheng, J., 2002: GCM experiments on changes in atmospheric predictability associated with the
791 PNA pattern and tropical SST anomalies. *Tellus*, **54A**, 317–329, doi: 10.1034/j.1600-
792 0870.2002.01324.x.
793 Strong, C., and R. E. Davis, 2008: Variability in the position and strength of winter jet stream
794 cores related to Northern Hemisphere teleconnections. *J. Climate*, **21**, 584–592, doi:
795 10.1175/2007JCLI1723.1.
796 Tibaldi, S., and F. Molteni, 1990: On the operational predictability of blocking. *Tellus*, **42A**,
797 343–365, doi: 10.1034/j.1600-0870.1990.t01-2-00003.x.
798 Thompson, D. W. J., and J. M. Wallace, 1998: The Arctic oscillation signature in wintertime
799 geopotential height and temperature fields. *Geophys. Res. Lett.*, **25**, 1297–1300, doi:
800 10.1029/98GL00950.
801 Torn, R. D., 2010: Diagnosis of the downstream ridging associated with extratropical transition
802 using short-term ensemble forecasts. *J. Atmos. Sci.*, **67**, 817–833, doi:
803 10.1175/2009JAS3093.1.
804 Torn, R. D., and G. J. Hakim, 2015: Comparison of wave packets associated with extratropical
805 transition and winter cyclones. *Mon. Wea. Rev.*, **143**, 1782–1803, doi: 10.1175/MWR-D-
806 14-00006.1.
807 Wallace, J. M., and D. S. Gutzler, 1981: Teleconnections in the geopotential height field during
808 the Northern Hemisphere winter. *Mon. Wea. Rev.*, **109**, 784–812, doi: 10.1175/1520-
809 0493(1981)109<0784:TITGHF>2.0.CO;2.
810 Wang, L., and W. Chen, 2014: An intensity index for the East Asian winter monsoon. *J. Climate*,
811 **27**, 2361–2374, doi: 10.1175/JCLI-D-13-00086.1.

812 Weare, B. C., and J. S. Nasstrom, 1982: Examples of extended empirical orthogonal function
813 analyses. *Mon. Wea. Rev.*, **110**, 481–485, doi:10.1175/1520-0493(1982)110,0481:
814 EOEEOF.2.0.CO;2.
815 Wettstein, J. J., and J. M. Wallace, 2010: Observed patterns of month-to-month storm-track
816 variability and their relationship to the background flow. *J. Atmos. Sci.*, **67**, 1420–1437,
817 doi: 10.1175/2009JAS3194.1.
818 Wilks, D. S., 2011: Statistical Methods in the Atmospheric Sciences. 3rd ed. Elsevier, 676 pp.
819 Woollings, T., A. Hannachi, and B. Hoskins, 2010: Variability of the North Atlantic eddy-driven
820 jet stream. *Quart. J. Roy. Meteor. Soc.*, **136**, 856–868, doi: 10.1002/qj.625.
821 Xie, Z., Y. Du, and S. Yang, 2015: Zonal extension and retraction of the subtropical westerly jet
822 stream and evolution of precipitation over East Asia and the western Pacific. *J. Climate*,
823 **28**, 6783–6798, doi: 10.1175/JCLI-D-14-00649.1.
824 Yang, S., K.-M. Lau, and K.-M. Kim, 2002: Variations of the East Asian jet stream and Asian–
825 Pacific–American winter climate anomalies. *J. Climate*, **15**, 306–325, doi: 10.1175/1520-
826 0442(2002)015<0306:VOTEAJ>2.0.CO;2.
827

Table Captions

TABLE 1. Characteristic residence times in days for each NPJ regime. The numbers in parentheses represent the number of analysis times characterized by each NPJ regime during 1979–2014 excluding the summer months (Jun–Aug).

TABLE 2. NPJ Phase Diagram characteristics derived from the CFSR for the periods characterized by the best and worst NPJ Phase Diagram medium-range forecasts with all quantities expressed in standard deviations. ΔPC 1 and ΔPC 2 represent the change in PC 1 and PC 2, respectively, during the 10-day period following the initialization of a best and worst forecast. Positive (negative) values for ΔPC 1 and ΔPC 2 represent an NPJ that undergoes a jet extension and poleward shift (jet retraction and equatorward shift), respectively. The average 10-day trajectory length corresponds to the average Euclidean distance traveled by the NPJ within the NPJ Phase Diagram during the 10-day period following the initialization of a best and worst forecast. Shorter trajectories correspond to a more persistent NPJ configuration compared to longer trajectories. Asterisks indicate that values associated with the best and worst forecasts are statistically significantly different at the 99.9% confidence level.

851 **Tables**

General NPJ Regime Characteristics				
NPJ Regime	Mean Residence Time (d)	Median Residence Time (d)	Maximum Residence Time (d)	Minimum Residence Time (d)
Jet Extension (N=5842)	3.85	2.50	27.25	0.25
Jet Retraction (N=5685)	3.70	2.75	34.00	0.25
Poleward Shift (N=6164)	3.58	2.75	18.00	0.25
Equatorward Shift (N=5437)	3.65	2.50	18.50	0.25
Origin (N=16212)	4.65	3.25	35.50	0.25

852

853 TABLE 1. Characteristic residence times in days for each NPJ regime. The numbers in
854 parentheses represent the number of analysis times characterized by each NPJ regime during
855 1979–2014 excluding the summer months (Jun–Aug).
856
857

858

859

860

861

862

863

864

Comparison of Best/Worst Forecast Periods					
	Avg. Start PC 1	Avg. Start PC 2	Avg. 10-d ΔPC 1	Avg. 10-d ΔPC 2	Avg. 10-d Traj. Length
Best Forecasts (N=475)	0.09*	0.04	0.09	0.16*	3.50*
Worst Forecasts (N=763)	–0.18*	–0.08	0.01	–0.21*	4.33*

TABLE 2. NPJ Phase Diagram characteristics derived from the CFSR for the periods characterized by the best and worst NPJ Phase Diagram medium-range forecasts with all quantities expressed in standard deviations. ΔPC 1 and ΔPC 2 represent the change in PC 1 and PC 2, respectively, during the 10-day period following the initialization of a best and worst forecast. Positive (negative) values for ΔPC 1 and ΔPC 2 represent an NPJ that undergoes a jet extension and poleward shift (jet retraction and equatorward shift), respectively. The average 10-day trajectory length corresponds to the average Euclidean distance traveled by the NPJ within the NPJ Phase Diagram during the 10-day period following the initialization of a best and worst forecast. Shorter trajectories correspond to a more persistent NPJ configuration compared to longer trajectories. Asterisks indicate that values associated with the best and worst forecasts are statistically significantly different at the 99.9% confidence level.

890 **Figure Captions**

891 FIG. 1. (a) September–May 250-hPa mean zonal wind is contoured in black every 10 m s^{-1}
892 above 30 m s^{-1}, and the regression of 250-hPa zonal wind anomaly data onto standardized PC 1
893 (i.e., EOF 1) is shaded in m s^{-1}. The variance of 250-hPa zonal wind during the cool season that
894 is explained by EOF 1 is listed in the top right of the panel. (b) As in (a), but for the regression of
895 250-hPa zonal wind anomaly data onto standardized PC 2 (i.e., EOF 2).

896

897 FIG. 2. (a) 250-hPa wind speed in m s^{-1} is shaded following the legend at 1800 UTC 11 February
898 2004. (b) The location of weighted PC 1 and PC 2 at 1800 UTC 11 February 2004 within the
899 NPJ Phase Diagram. (c),(d) As in (a),(b) but for 1800 UTC 13 March 2009.

900

901 FIG. 3. As in Fig. 2, but for (a),(b) 1800 UTC 9 April 1984 and (c),(d) 1200 UTC 28 January
902 1991.

903

904 FIG. 4. Schematic illustrating the classification scheme for CFSR analysis times and GEFS
905 reforecasts with respect to the NPJ Phase Diagram.

906

907 FIG. 5. Composite mean 250-hPa wind speed in m s^{-1} is shaded in the fill pattern, 250-hPa
908 geopotential height is contoured in black every 120 m, and 250-hPa geopotential height
909 anomalies are contoured in solid red and dashed blue every 30 m for positive and negative
910 values, respectively, 4 days following the initiation of (a) a jet extension, (c) a jet retraction, (e) a
911 poleward shift, and (g) an equatorward shift regime. Composite anomalies of mean sea-level
912 pressure are contoured in solid and dashed black every 2 hPa for positive and negative values,

913 respectively, and 850-hPa temperature anomalies are shaded in the fill pattern every 1 K 4 days
914 following the initiation of (b) a jet extension, (d) a jet retraction, (f) a poleward shift, and (h) an
915 equatorward shift regime. The numbers in the bottom right of each panel indicate the number of
916 cases included in each composite. Stippled areas represent locations where the 250-hPa
917 geopotential height anomalies or 850-hPa temperature anomalies are statistically distinct from
918 climatology at the 99% confidence level.
919
920 FIG. 6. (a) The percent frequency of analysis times during every cool season between September
921 1979 and May 2014 that are characterized by each NPJ regime. The years indicated on the
922 horizontal axis identify the end of individual cool seasons. (b) The percent frequency of analysis
923 times during each month of the cool season that are characterized by each NPJ regime. The
924 numbers in parentheses below each month indicate the number of analysis times during each
925 month. The percentage in parentheses below a particular month identifies the amount of variance
926 explained by the first two EOFs of 250-hPa zonal wind anomaly data during three-month period
927 centered on that particular month between 1979 and 2014.
928
929 FIG. 7. (a) The percent frequency of each NPJ regime at analysis times during which the NPJ is
930 outside of the unit circle on the NPJ Phase Diagram and characterized by each phase of the PNA
931 discussed in the text. The numbers in parentheses below each category indicate the number of
932 analysis times in each category. (b) As in (a), but for the AO. (c) As in (a), but for ENSO.
933
934 FIG. 8. (a) The average percent distance error of GEFS ensemble mean NPJ Phase Diagram
935 forecasts initialized during the same season relative to the average distance error of all ensemble

936 mean NPJ Phase Diagram forecasts initialized during the cool season. Positive (negative)
937 average percent errors correspond to average errors that are greater than (less than) the cool
938 season average. The numbers immediately above the horizontal axis identify the average
939 distance error in standard deviations for all ensemble mean NPJ Phase Diagram forecasts at a
940 particular lead time. The colored circles on each line indicate that the error associated with that
941 season is statistically distinct from the error associated with another season at the 99%
942 confidence level (e.g., a red circle on the line corresponding to winter indicates that the error
943 associated with forecasts during the winter is statistically distinct from the error associated with
944 forecasts during the fall at that lead time). The numbers in parentheses in the legend indicate the
945 number of forecasts in that category. Forecast lead time on the horizontal axis represents the
946 hours after forecast initialization. (b) As in (a), but for forecasts initialized during the same NPJ
947 regime. (c) As in (a), but for forecasts verified during the same NPJ regime. Forecast lead time
948 on the horizontal axis in (c) depicts the hours prior to forecast verification.
949
950 FIG. 9. The percent frequency that an NPJ regime is overforecast or underforecast by the GEFS
951 ensemble mean NPJ Phase Diagram forecasts relative to the verifying 0-h analyses at each
952 forecast lead time.
953
954 FIG. 10. Schematic illustrating the classification scheme for the best and worst NPJ Phase
955 Diagram medium-range forecasts. (a),(b) The top row identifies a series of accurate forecasts that
956 vary in their level of precision, while (c),(d) the bottom row identifies a series of inaccurate
957 forecasts that vary in their level of precision.
958

959 FIG. 11. (a) The percent frequency of the best and worst NPJ Phase Diagram medium-range
960 forecasts that are initialized during each month of the cool season. (b) The percent frequency of
961 the best and worst NPJ Phase Diagram medium-range forecasts that are initialized during each
962 NPJ regime.
963
964 FIG. 12. Composite mean 250-hPa wind speed in m s^{-1} is shaded in the fill pattern, 250-hPa
965 geopotential height is contoured in black every 120 m, and 250-hPa geopotential height
966 anomalies are contoured in solid red and dashed blue every 30 m for positive and negative
967 values, respectively, at the time (a) a best and (b) a worst NPJ Phase Diagram forecast is
968 initialized during a jet extension. (c),(d) As in (a),(b), but for those forecasts that are initialized
969 during a jet retraction. (e),(f) As in (a),(b), but for those forecasts that are initialized during a
970 poleward shift. (g),(h) As in (a),(b), but for those forecasts that are initialized during an
971 equatorward shift. The quantities in the top right corner of every panel indicate the number of
972 cases included in each composite.
973
974 FIG. 13. (a) The difference between the 250-hPa geopotential height anomalies associated with a
975 worst and best NPJ Phase Diagram forecast at the time of forecast initialization during a jet
976 extension is shaded every 30 m in the fill pattern. (b) As in (a), but during a jet retraction. (c) As
977 in (a), but during a poleward shift. (d) As in (a), but during an equatorward shift. Statistically
978 significant differences in geopotential height anomalies at the 99% confidence level are stippled
979 in all panels.
980

FIG. 14. As in Fig. 13, but for the composite 250-hPa flow patterns 192 h following the initialization of a best and worst NPJ Phase Diagram forecast.

FIG. 15. As in Fig. 14, but for the composite difference between 250-hPa geopotential height anomalies 192 h following the initialization of a worst and best NPJ Phase Diagram forecast.

Figures

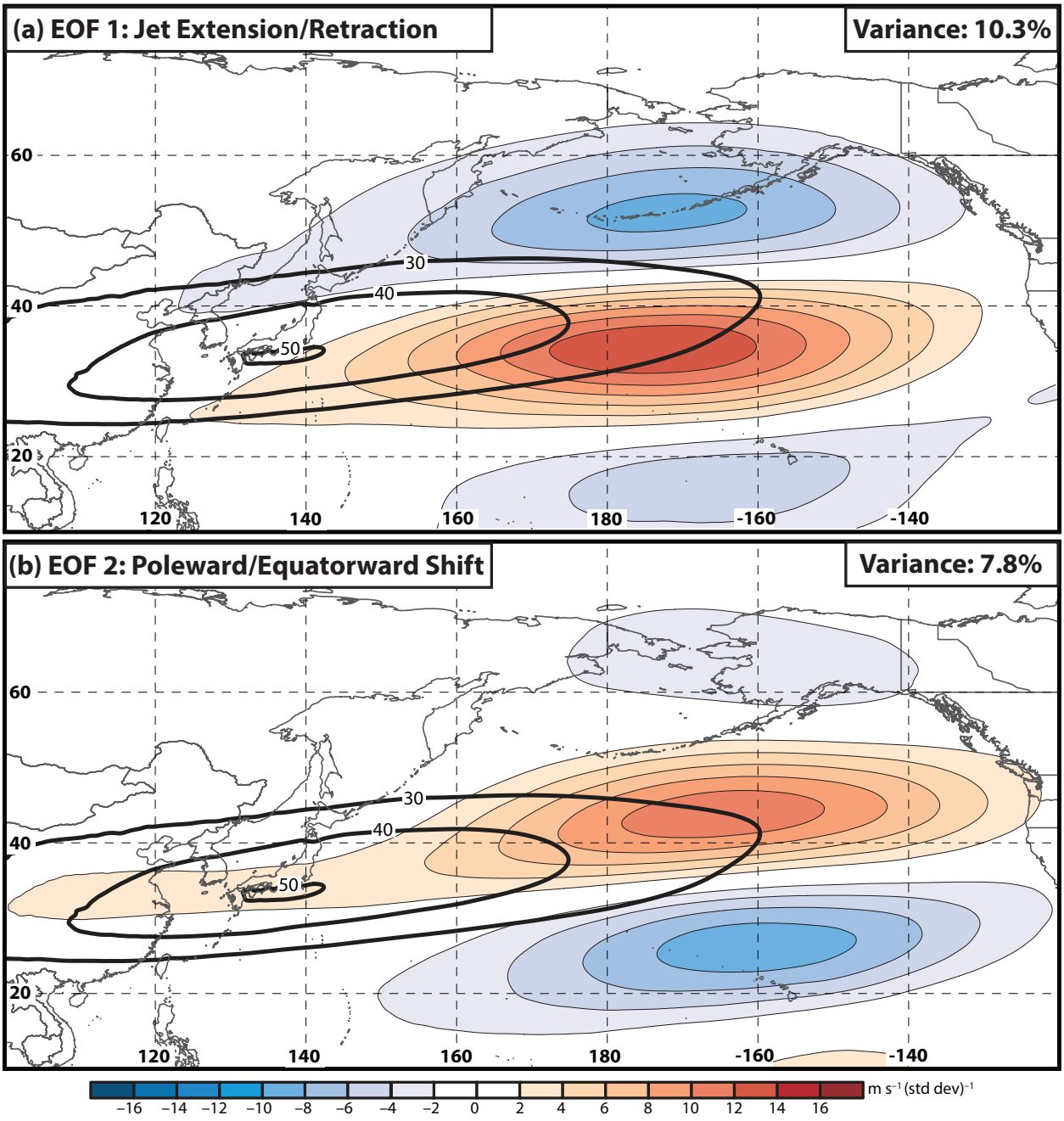

FIG. 1. (a) September–May 250-hPa mean zonal wind is contoured in black every 10 m s–1 above 30 m s–1, and the regression of 250-hPa zonal wind anomaly data onto standardized PC 1 (i.e., EOF 1) is shaded in m s–1. The variance of 250-hPa zonal wind during the cool season that is explained by EOF 1 is listed in the top right of the panel. (b) As in (a), but for the regression of 250-hPa zonal wind anomaly data onto standardized PC 2 (i.e., EOF 2).

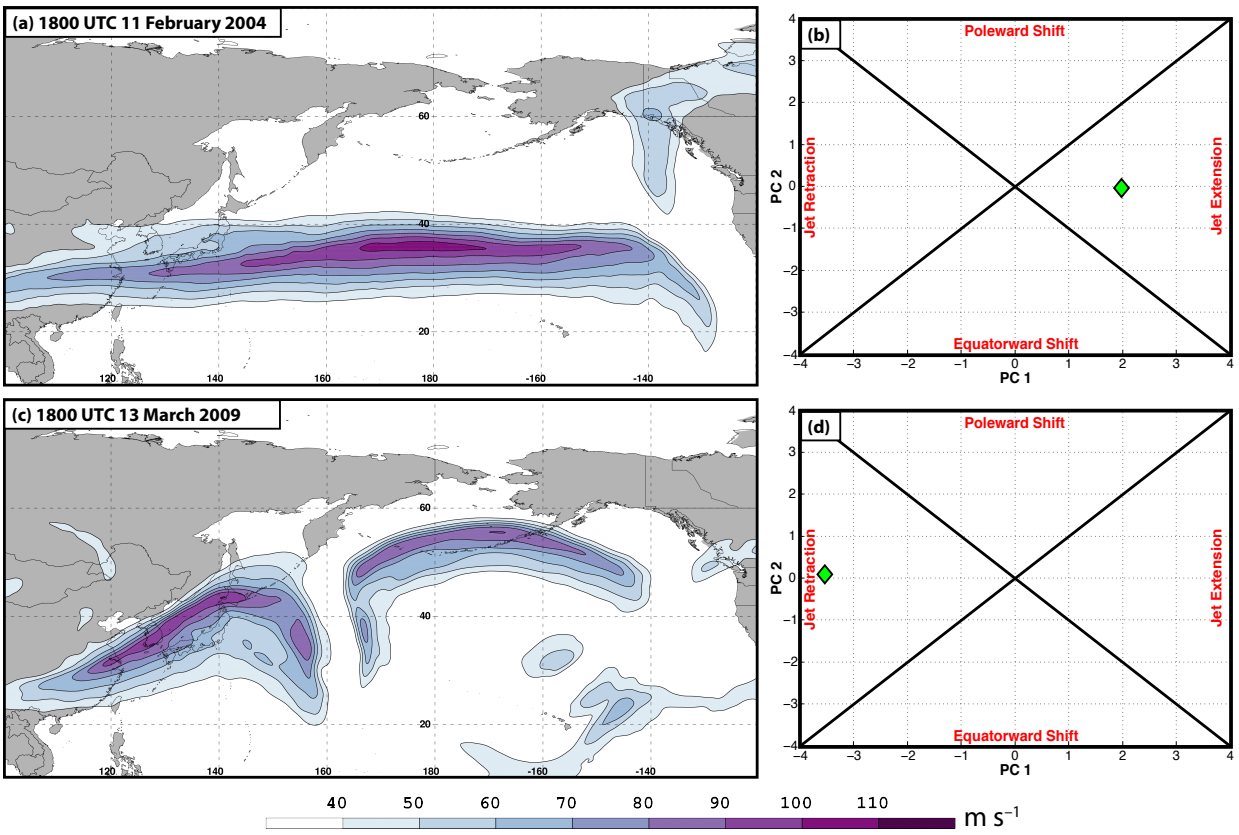

FIG. 2. (a) 250-hPa wind speed in m s–1 is shaded following the legend at 1800 UTC 11 February 2004. (b) The location of weighted PC 1 and PC 2 at 1800 UTC 11 February 2004 within the NPJ Phase Diagram. (c),(d) As in (a),(b) but for 1800 UTC 13 March 2009.

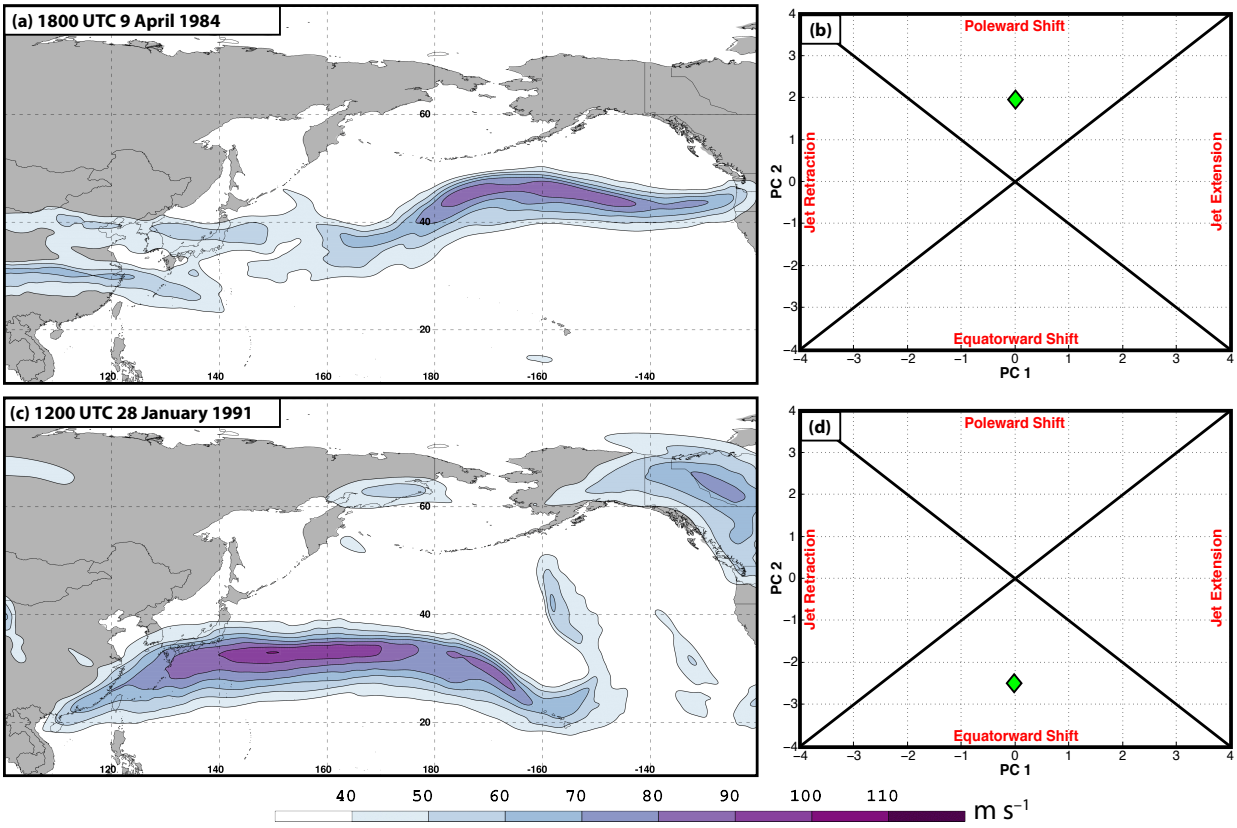

FIG. 3. As in Fig. 2, but for (a),(b) 1800 UTC 9 April 1984 and (c),(d) 1200 UTC 28 January 1991.

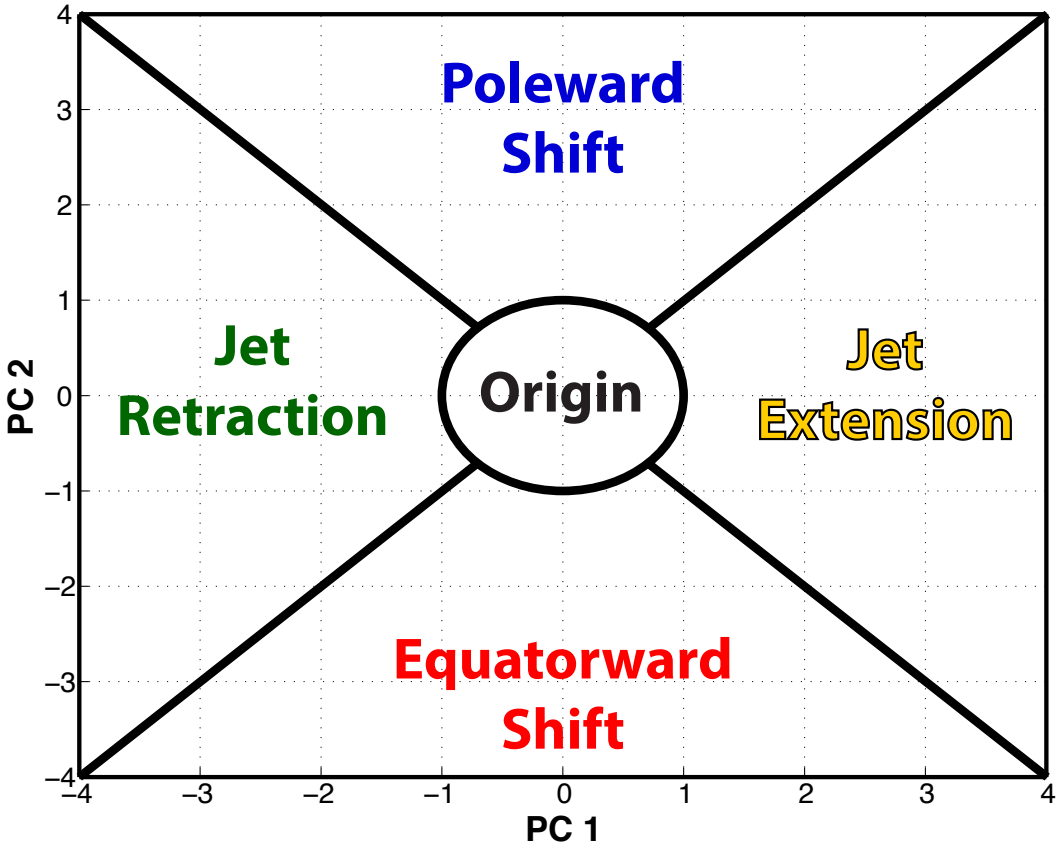

FIG. 4. Schematic illustrating the classification scheme for CFSR analysis times and GEFS reforecasts with respect to the NPJ Phase Diagram.

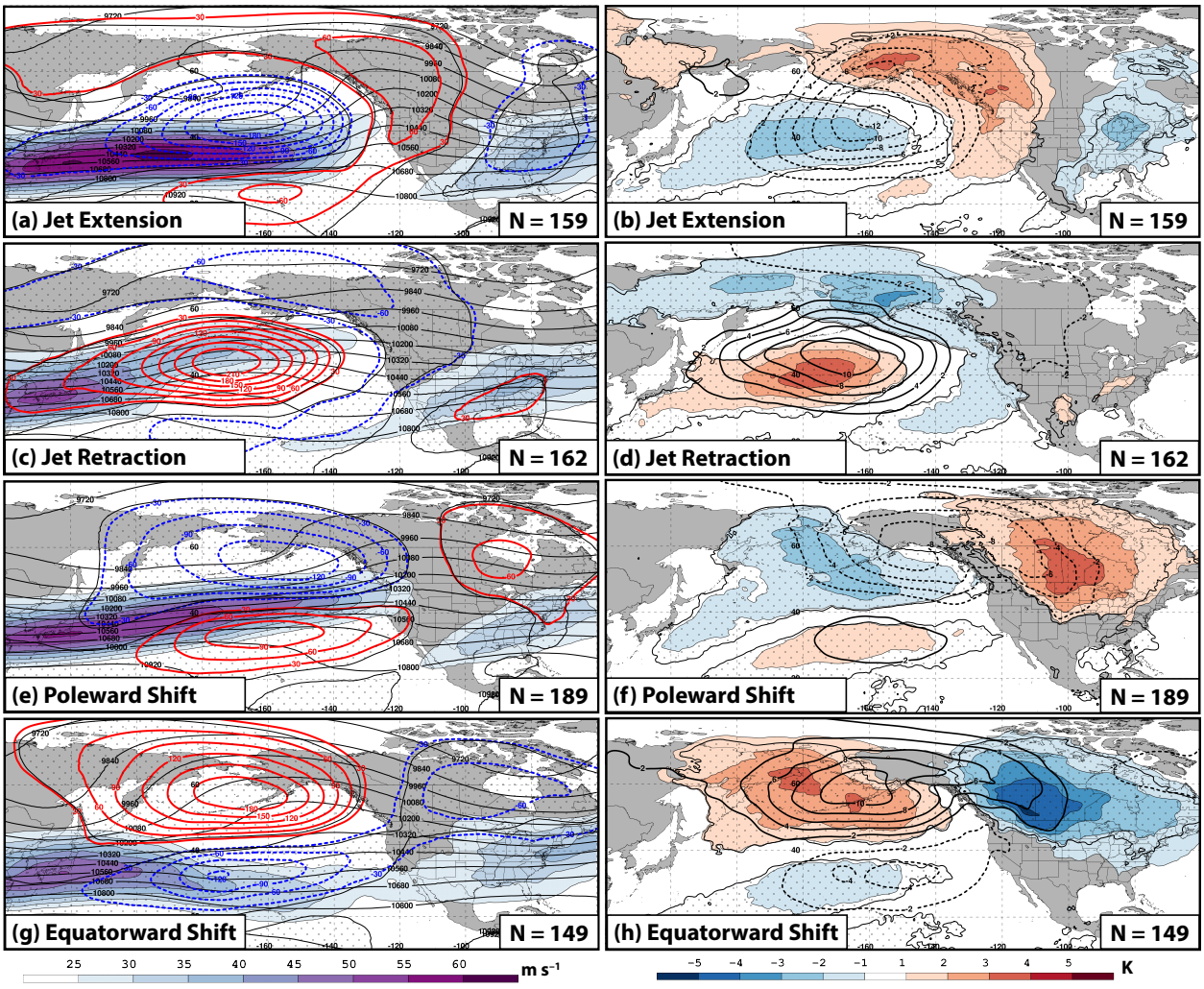

FIG. 5. Composite mean 250-hPa wind speed in m s–1 is shaded in the fill pattern, 250-hPa geopotential height is contoured in black every 120 m, and 250-hPa geopotential height anomalies are contoured in solid red and dashed blue every 30 m for positive and negative values, respectively, 4 days following the initiation of (a) a jet extension, (c) a jet retraction, (e) a poleward shift, and (g) an equatorward shift regime. Composite anomalies of mean sea-level pressure are contoured in solid and dashed black every 2 hPa for positive and negative values, respectively, and 850-hPa temperature anomalies are shaded in the fill pattern every 1 K 4 days following the initiation of (b) a jet extension, (d) a jet retraction, (f) a poleward shift, and (h) an equatorward shift regime. The numbers in the bottom right of each panel indicate the number of cases included in each composite. Stippled areas represent locations where the 250-hPa geopotential height anomalies or 850-hPa temperature anomalies are statistically distinct from climatology at the 99% confidence level.

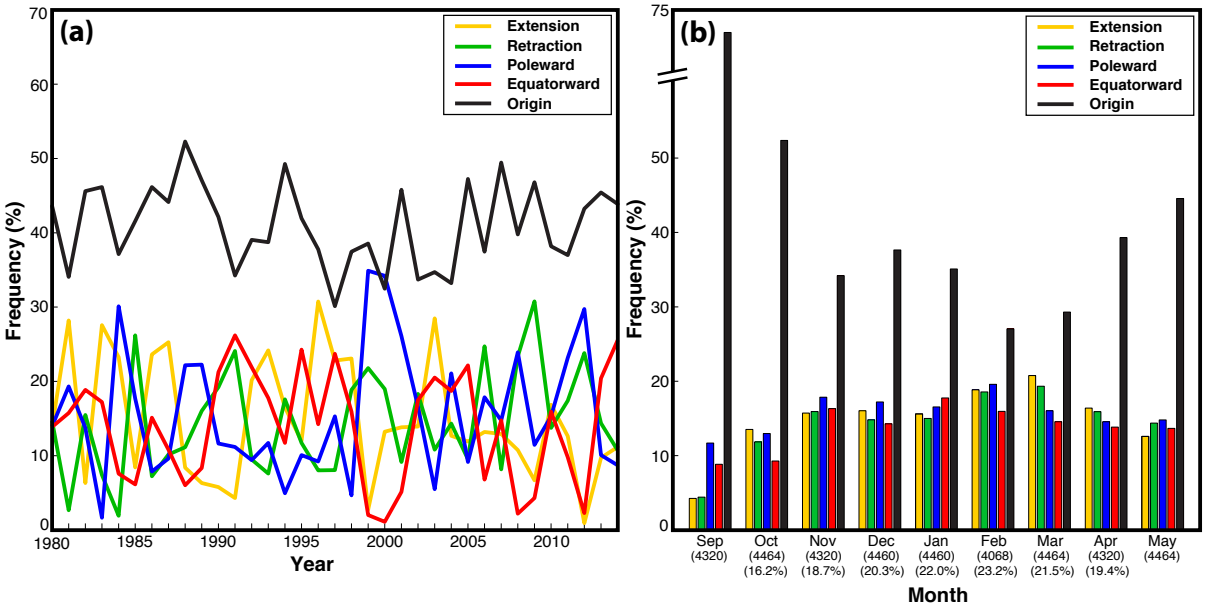

FIG. 6. (a) The percent frequency of analysis times during every cool season between September 1979 and May 2014 that are characterized by each NPJ regime. The years indicated on the horizontal axis identify the end of individual cool seasons. (b) The percent frequency of analysis times during each month of the cool season that are characterized by each NPJ regime. The numbers in parentheses below each month indicate the number of analysis times during each month. The percentage in parentheses below a particular month identifies the amount of variance explained by the first two EOFs of 250-hPa zonal wind anomaly data during three-month period centered on that particular month between 1979 and 2014.

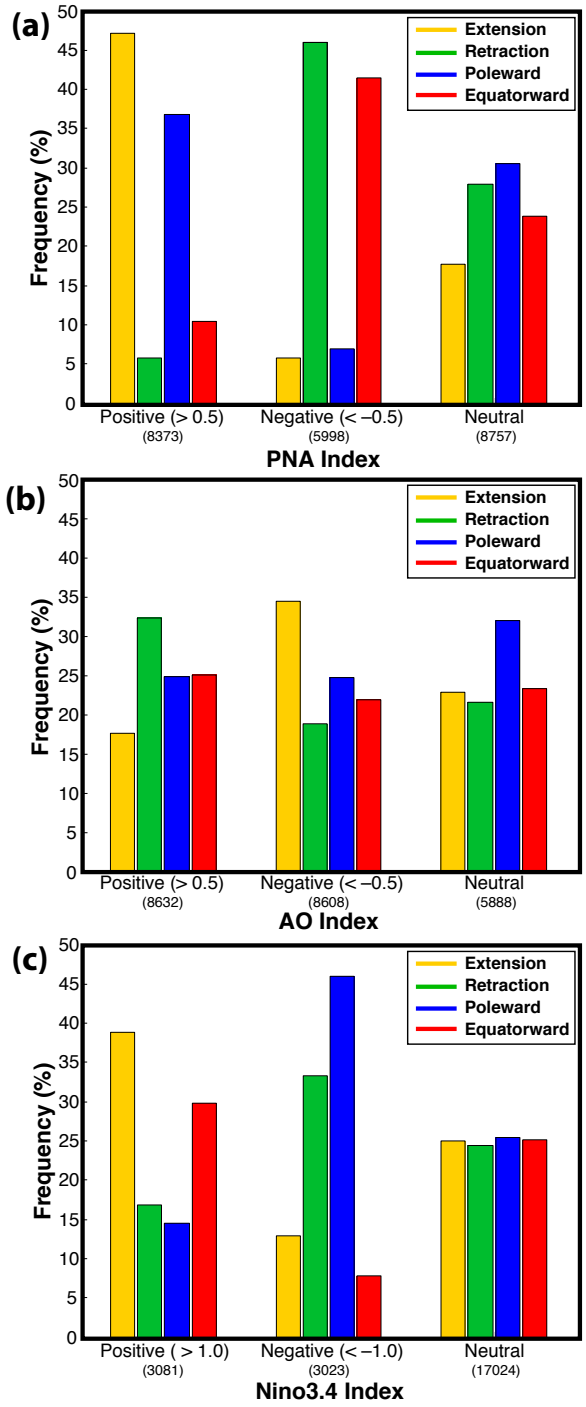

FIG. 7. (a) The percent frequency of each NPJ regime at analysis times during which the NPJ is outside of the unit circle on the NPJ Phase Diagram and characterized by each phase of the PNA discussed in the text. The numbers in parentheses below each category indicate the number of analysis times in each category. (b) As in (a), but for the AO. (c) As in (a), but for ENSO.

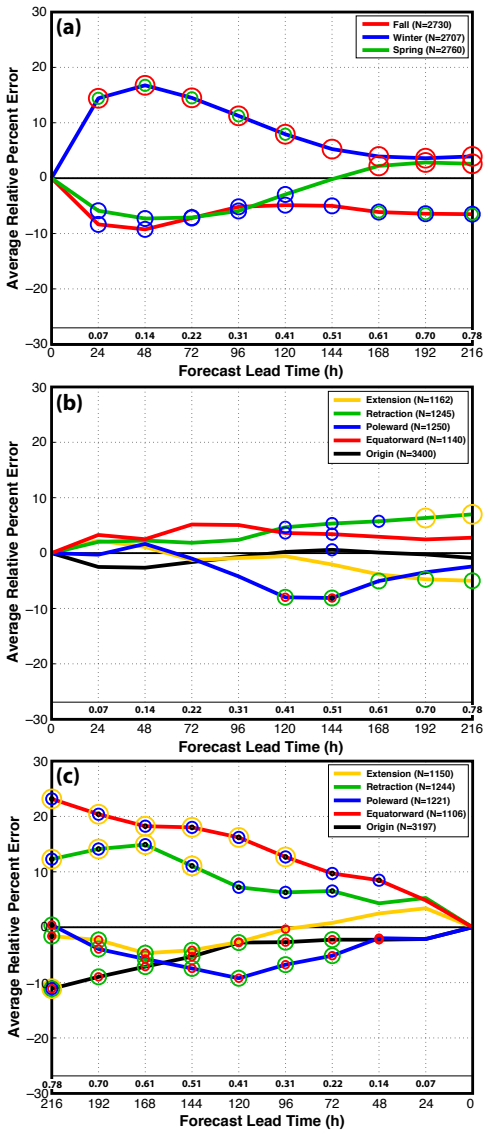

FIG. 8. (a) The average percent distance error of GEFS ensemble mean NPJ Phase Diagram forecasts initialized during the same season relative to the average distance error of all ensemble mean NPJ Phase Diagram forecasts initialized during the cool season. Positive (negative) average percent errors correspond to average errors that are greater than (less than) the cool season average. The numbers immediately above the horizontal axis identify the average distance error in standard deviations for all ensemble mean NPJ Phase Diagram forecasts at a particular lead time. The colored circles on each line indicate that the error associated with that season is statistically distinct from the error associated with another season at the 99% confidence level (e.g., a red circle on the line corresponding to winter indicates that the error associated with forecasts during the winter is statistically distinct from the error associated with forecasts during the fall at that lead time). The numbers in parentheses in the legend indicate the number of forecasts in that category. Forecast lead time on the horizontal axis represents the hours after forecast initialization. (b) As in (a), but for forecasts initialized during the same NPJ regime. (c) As in (a), but for forecasts verified during the same NPJ regime. Forecast lead time on the horizontal axis in (c) depicts the hours prior to forecast verification.

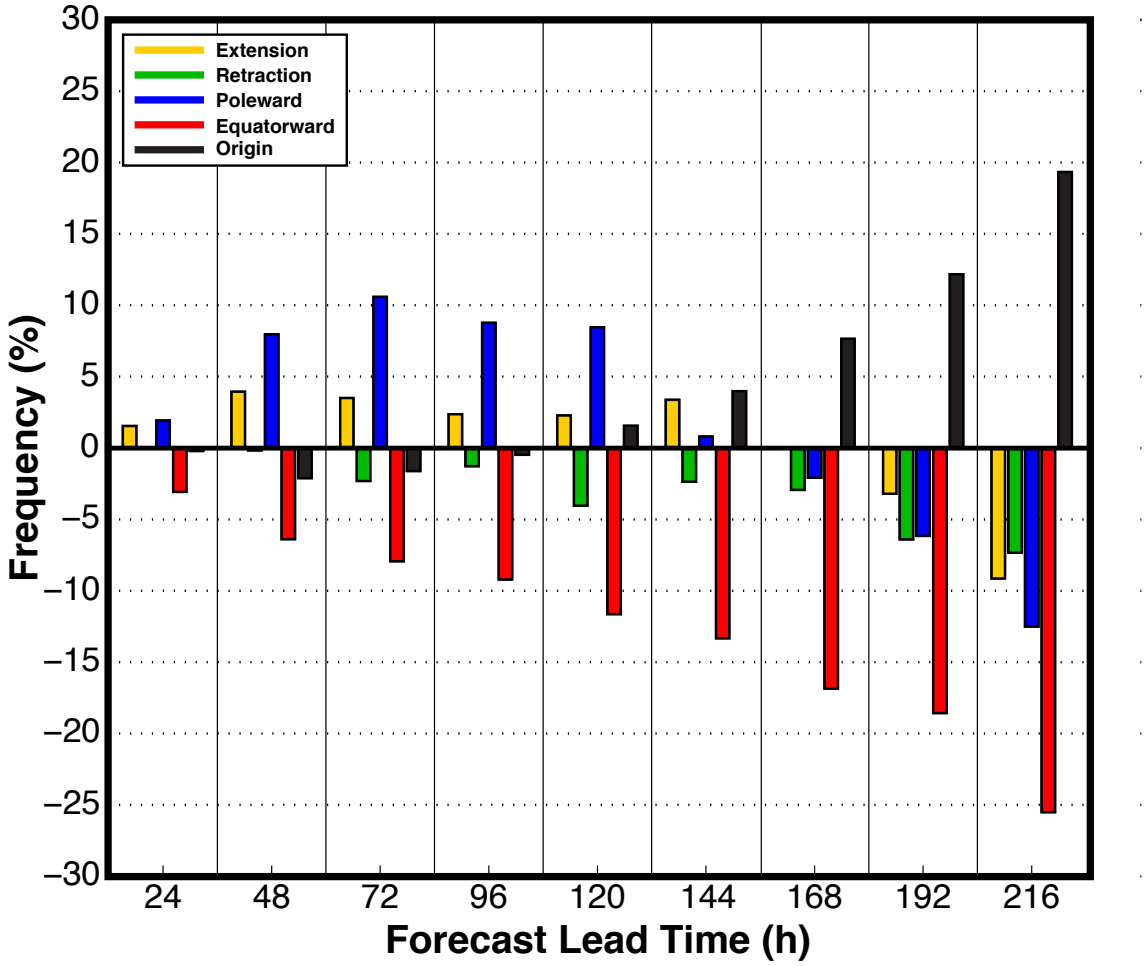

FIG. 9. The percent frequency that an NPJ regime is overforecast or underforecast by the GEFS ensemble mean NPJ Phase Diagram forecasts relative to the verifying 0-h analyses at each forecast lead time.

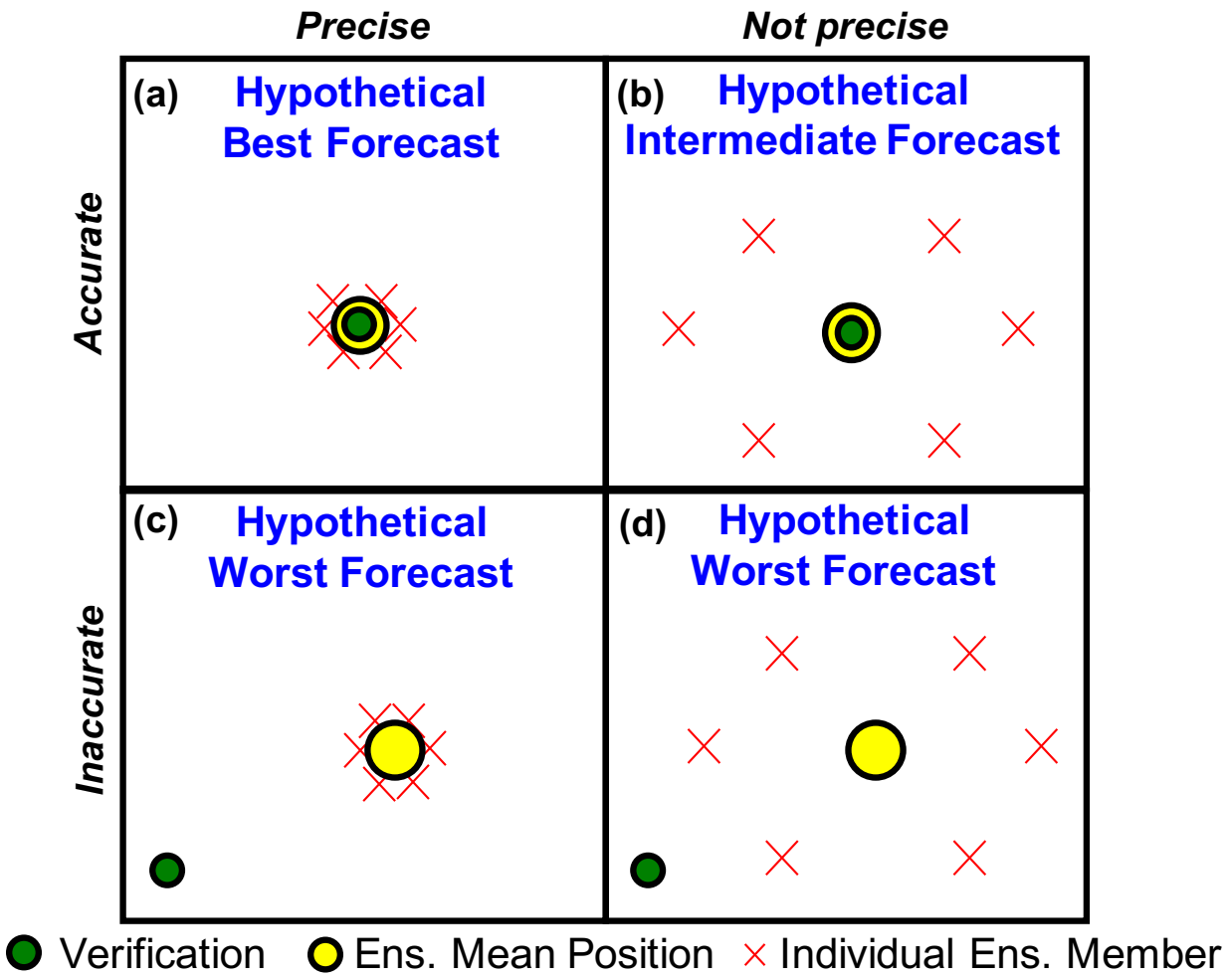

FIG. 10. Schematic illustrating the classification scheme for the best and worst NPJ Phase Diagram medium-range forecasts. (a),(b) The top row identifies a series of accurate forecasts that vary in their level of precision, while (c),(d) the bottom row identifies a series of inaccurate forecasts that vary in their level of precision.

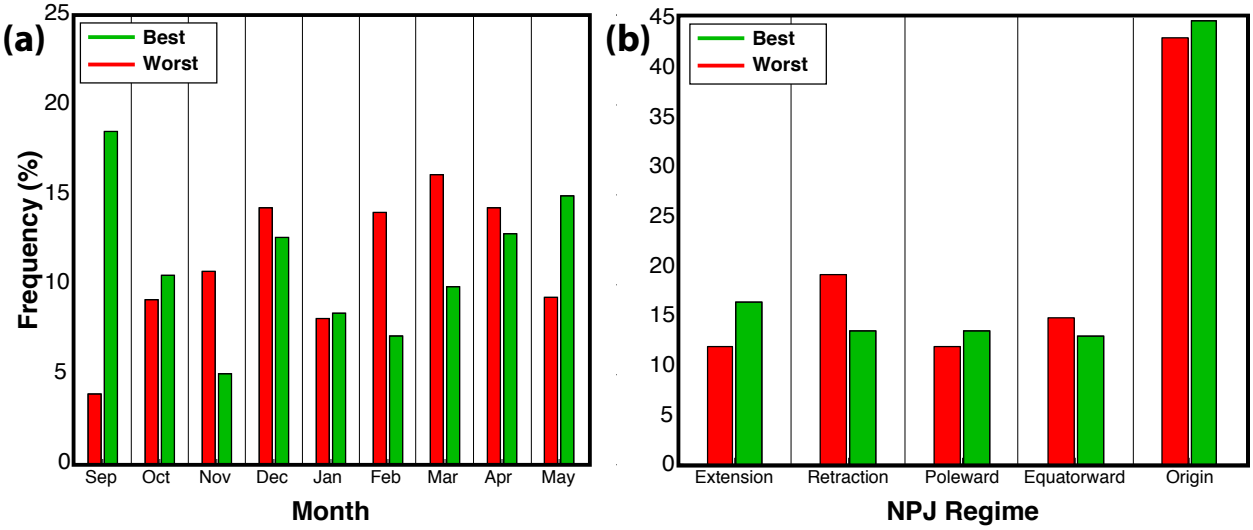

FIG. 11. (a) The percent frequency of the best and worst NPJ Phase Diagram medium-range forecasts that are initialized during each month of the cool season. (b) The percent frequency of the best and worst NPJ Phase Diagram medium-range forecasts that are initialized during each NPJ regime.

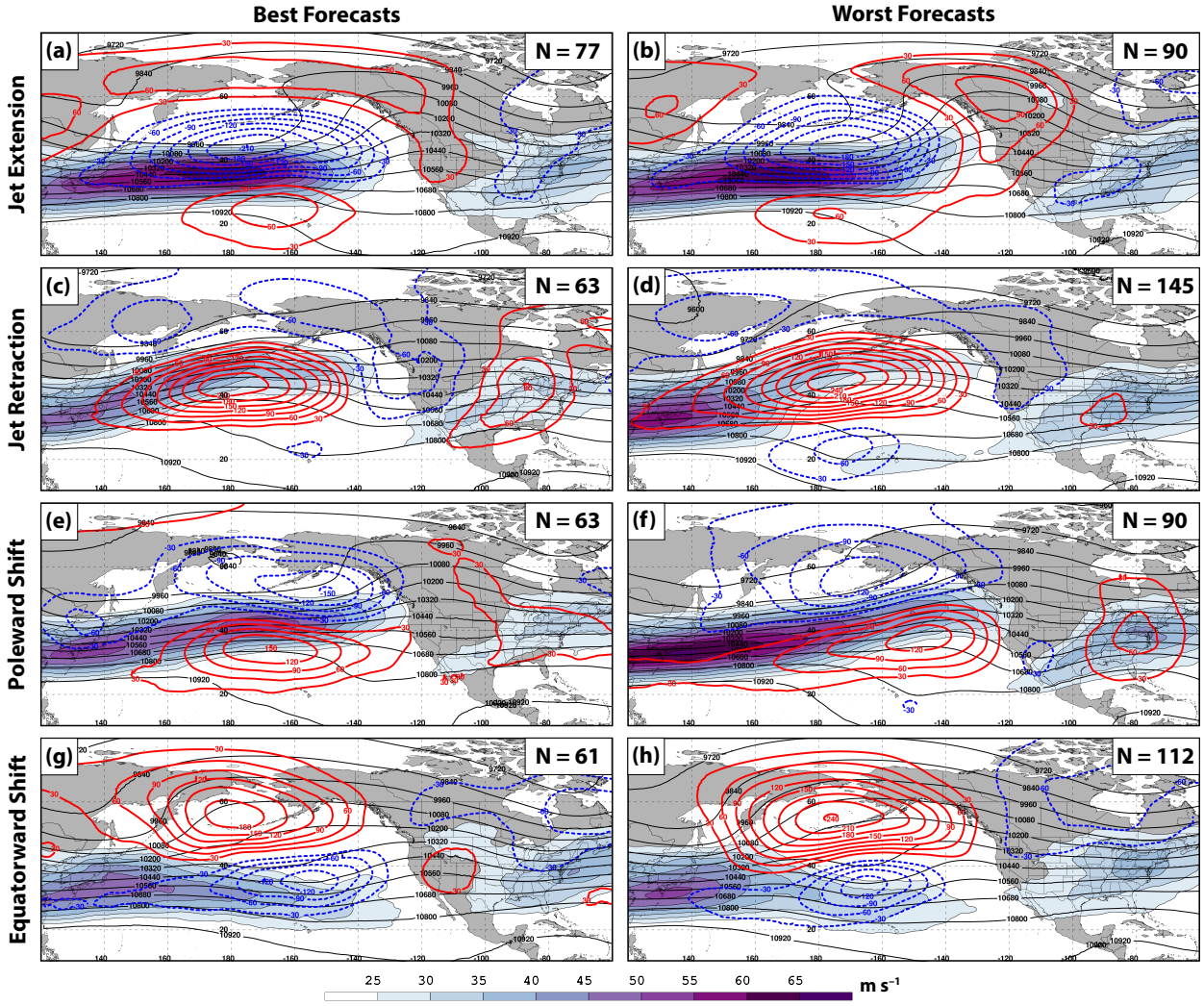

FIG. 12. Composite mean 250-hPa wind speed in m s–1 is shaded in the fill pattern, 250-hPa geopotential height is contoured in black every 120 m, and 250-hPa geopotential height anomalies are contoured in solid red and dashed blue every 30 m for positive and negative values, respectively, at the time (a) a best and (b) a worst NPJ Phase Diagram forecast is initialized during a jet extension. (c),(d) As in (a),(b), but for those forecasts that are initialized during a jet retraction. (e),(f) As in (a),(b), but for those forecasts that are initialized during a poleward shift. (g),(h) As in (a),(b), but for those forecasts that are initialized during an equatorward shift. The quantities in the top right corner of every panel indicate the number of cases included in each composite.

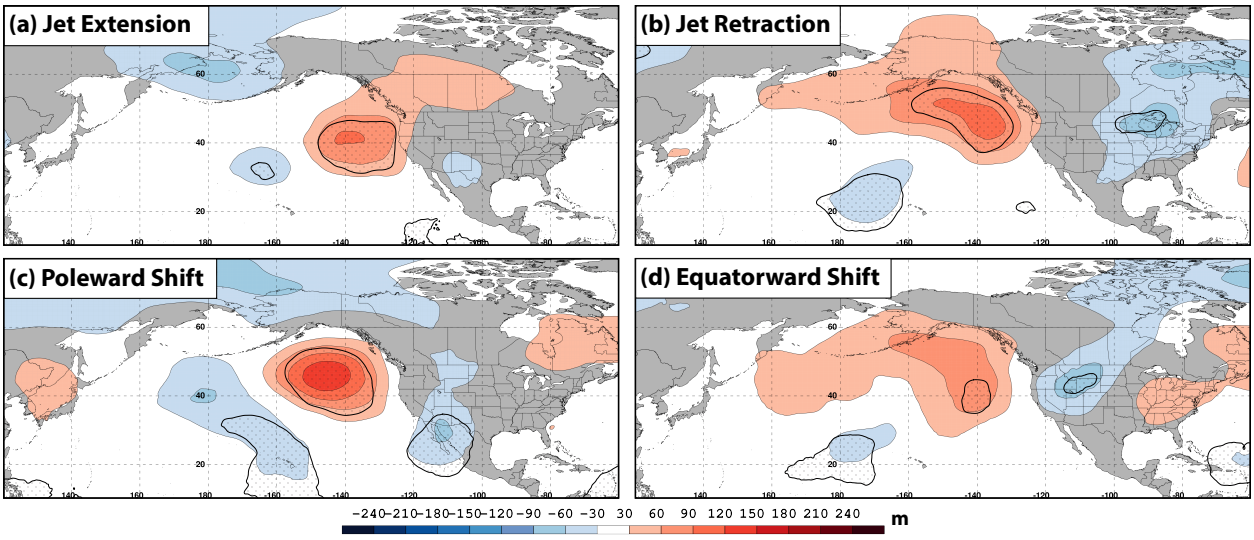

FIG. 13. (a) The difference between the 250-hPa geopotential height anomalies associated with a worst and best NPJ Phase Diagram forecast at the time of forecast initialization during a jet extension is shaded every 30 m in the fill pattern. (b) As in (a), but during a jet retraction. (c) As in (a), but during a poleward shift. (d) As in (a), but during an equatorward shift. Statistically significant differences in geopotential height anomalies at the 99% confidence level are stippled in all panels.

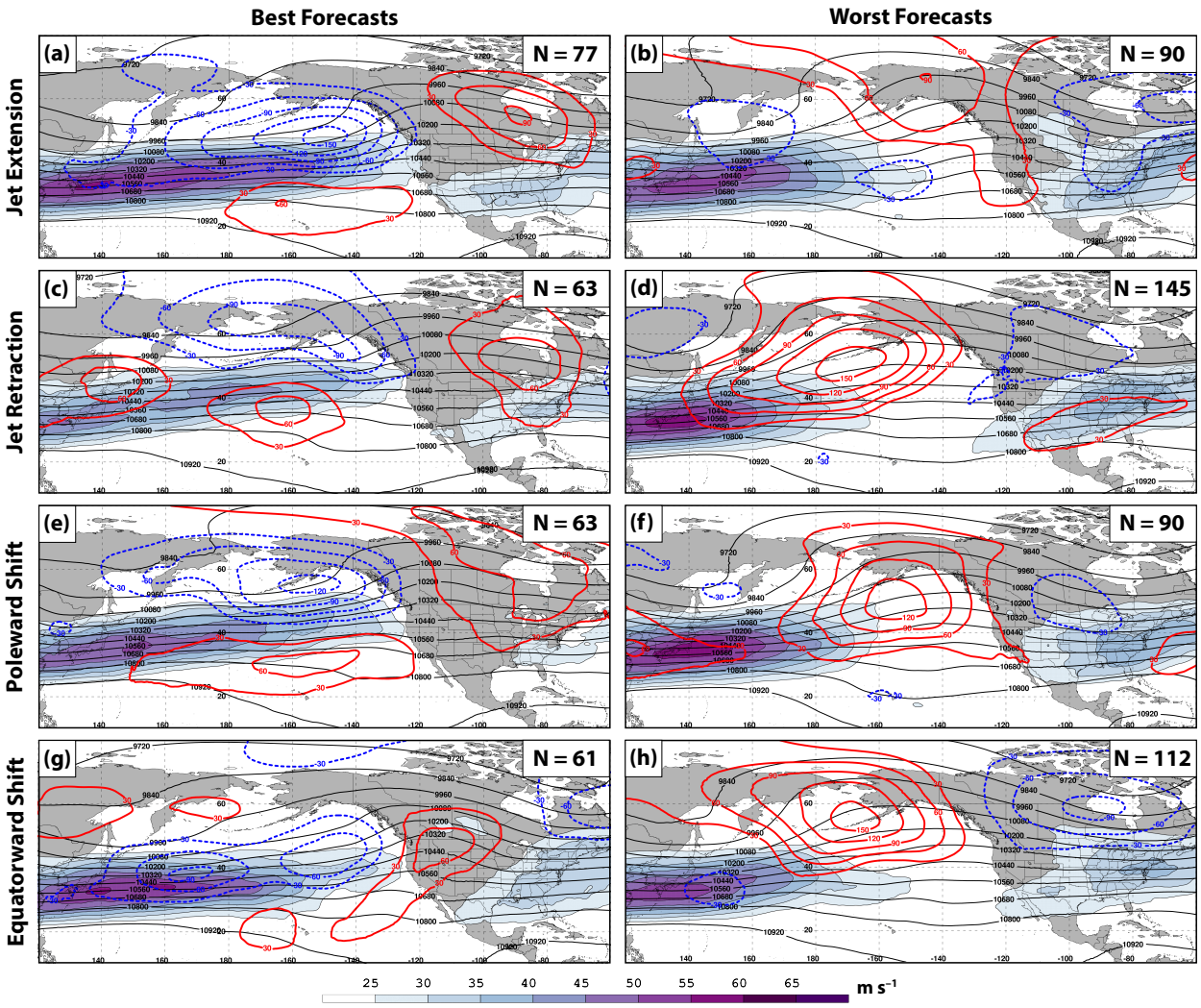

FIG. 14. As in Fig. 13, but for the composite 250-hPa flow patterns 192 h following the initialization of a best and worst NPJ Phase Diagram forecast.

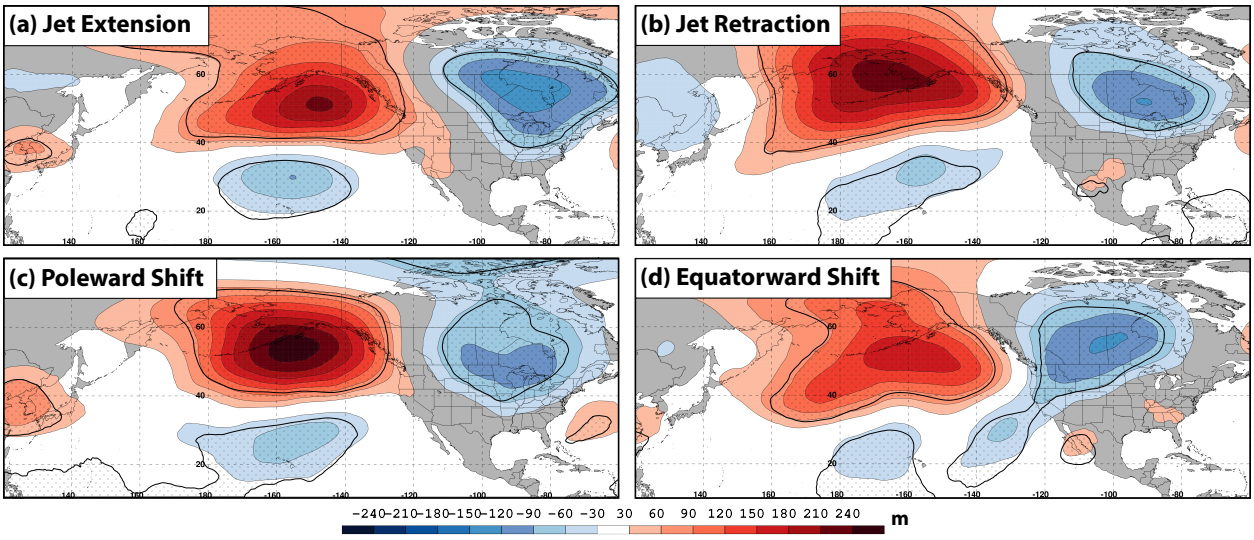

FIG. 15. As in Fig. 14, but for the composite difference between 250-hPa geopotential height anomalies 192 h following the initialization of a worst and best NPJ Phase Diagram forecast.